https://doi.org/10.5194/essd-2026-94
Preprint. Discussion started: 2 March 2026

Extended global terrestrial evapotranspiration and gross primary production dataset from 1982 to near present

Zhenwu Xu[1], Yongqiang Zhang[1], Dongdong Kong[2], Ning Ma[1], Xuanze Zhang[1]

[1]Key Laboratory of Water Cycle and Related Land Surface Processes, Institute of Geographic Sciences and Natural Resources Research, Chinese Academy of Sciences, Beijing, 100101, China
[2]Department of Atmospheric Science, School of Environmental Studies, China University of Geosciences, Wuhan, 430074, China

Correspondence to: Yongqiang Zhang (zhangyq@igsnrr.ac.cn)

Abstract. The Penman–Monteith–Leuning (PML) model is a widely recognized diagnostic framework for estimating coupled terrestrial evapotranspiration (ET) and gross primary production (GPP). To address the critical need for high-fidelity, long-term, and near-present eco-hydrological records, we developed the PML-V2.2 dataset, spanning from 1982 to 2024. Driven by observation-constrained Multi-Source Weighted-Ensemble Precipitation (MSWEP) and Multi-Source Weather (MSWX) meteorological variables, the dataset comprises three complementary products: (1) PML-V2.2a, an 8-day 500 m MODIS-based product (2000–2024) optimized for near-present monitoring; (2) PML-V2.2b, a half-month 0.1° AVHRR-based product (1982–2020) anchoring long-term climate attribution; and (3) PML-V2.2c, a consolidated half-month 0.1° record integrating the former two for seamless 43-year continuity (1982–2024). Our methodological framework features an expanded bottom-up calibration using 208 flux sites (~1400 site-years) across various plant functional types (PFT) and a refined parameterization that explicitly distinguishes between irrigated and rainfed croplands. This distinction effectively mitigated systematic biases in agricultural regions, reducing ET and GPP estimation errors by 8.7% and 16.2%, respectively. Performance evaluation reveals high accuracy across PFTs (cross-validation Nash-Sutcliffe Efficiency, NSE > 0.60, absolute bias < 5%), while top-down water-balance validation across 56 large river basins during 1982–2016 and 152 basins during 2003–2020 confirms exceptional reliability (NSE: 0.89–0.91). The MODIS-based (V2.2a) and AVHRR-based (V2.2b) products exhibit high statistical and spatial agreement during their overlapping period (NSE = 0.90 and 0.79 for annual ET and GPP anomalies), ensuring a seamless transition across satellite epochs. Based on the consolidated PML-V2.2c dataset, global terrestrial annual ET and GPP during 1982–2024 are estimated at 65.8×10^3 km^3 yr^{-1} (with 58.0% from transpiration) and 143.0 PgC yr^{-1}, respectively. Long-term analysis reveals significant ($p < 0.01$) increasing trends in GPP (0.315 PgC yr^{-2}) and ET (0.019×10^3 km^3 yr^{-2}) during 1982–2024, where rapid growth in GPP and water use efficiency is partially offset by CO_2-induced physiological water savings. By bridging the gap between satellite epochs, PML-V2.2 provides an internally consistent long-term global dataset for hydrology, ecology, and other Earth science studies. The dataset is freely accessible, with the 500 m resolution PML-V2.2a product hosted on Google Earth Engine, and all 0.1° PML-V2.2a/b/c versions archived at the National Tibetan Plateau Data Center under https://doi.org/10.11888/Terre.tpdc.303314 (Xu et al., 2026).

https://doi.org/10.5194/essd-2026-94
Preprint. Discussion started: 2 March 2026

Open Access Earth System Science Data Discussions

1 Introduction

Terrestrial evapotranspiration (ET), the primary pathway for water transfer from the land surface to the atmosphere, plays a pivotal role in regulating Earth's hydrological cycle and energy balance (Oki, 2006; Zhang et al., 2026). As a fundamental driver of surface-atmosphere interactions, ET dictates the partitioning of net radiation into latent and sensible heat fluxes, thereby modulating surface temperatures, boundary layer dynamics, and global atmospheric circulation. Beyond its physical impact, ET serves as a critical bridge between the water and carbon cycles via transpiration, which is coupled with gross primary productivity (GPP) through stomatal regulation. This mechanism inherently governs ecosystem water use efficiency (WUE) (Zhang et al., 2022; Li et al., 2023b; Yuan et al., 2025b). Furthermore, ET acts as a major moisture source for terrestrial precipitation (P) through moisture recycling processes—a feedback increasingly critical in a greening Earth (Hoek van Dijke et al., 2022; Cui et al., 2022; Yang et al., 2023). Given these multifaceted roles, the development of accurate, long-term, and spatially consistent ET and GPP datasets is imperative for addressing the escalating challenges in climate, hydrological, and ecological sciences amidst global warming, precipitation shifts, and vegetation changes (Zhang et al., 2016a; Zhao et al., 2022b; Zhang et al., 2023).

The increasing availability of satellite observations and the maturation of land surface modeling have fostered a diverse ecosystem of remote-sensing-based diagnostic ET and GPP products. Table 1 synthesizes current models, focusing on datasets with a spatial resolution of 0.25° or finer to ensure the spatial fidelity required for detailed regional and global assessments. Unlike prognostic land surface models (LSMs), these diagnostic frameworks directly assimilate satellite-derived vegetation dynamics (e.g., leaf area index, LAI) to circumvent the systematic biases often inherent in complex plant functional type (PFT) simulations. Broadly, these datasets can be categorized into three primary clusters based on their target variables: (1) stand-alone ET algorithms rooted in Penman-Monteith (e.g., MOD16) or energy/water-balance principles (e.g., 3T, SiTH); (2) GPP-specific products driven largely by Light Use Efficiency (LUE) logic (e.g., MOD17, GLASS) or emerging proxies like SIF and NIRv (e.g., GOSIF); and (3) integrated frameworks that simultaneously estimate both fluxes to ensure physiological consistency (e.g., BEPS, BESS). Notably, within these categories, Machine Learning (ML) has emerged as a transformative force. This includes pure data-driven approaches that upscale flux observations directly (e.g., FLUXCOM-X-BASE, GloFlux) and hybrid strategies that embed ML into process-based schemes to refine specific parameters like stress factors (e.g., GLEAM4, CoSEB).

Despite this methodological diversity, the current data landscape is characterized by a persistent trade-off between temporal depth and biophysical consistency. This dichotomy is largely dictated by the evolution of satellite sensors: while higher-resolution diagnostic records are predominantly tethered to the post-2000 era of the Moderate Resolution Imaging Spectroradiometer (MODIS), establishing pre-2000 baselines necessitates reliance on the Advanced Very High Resolution Radiometer (AVHRR). However, bridging these distinct epochs is difficult, and many long-term datasets covering earlier decades estimate ET and GPP in isolation. This challenge is further compounded by instabilities in meteorological driving data (e.g., solar radiation, vapor pressure deficit) derived from disparate reanalysis products, which collectively increase the

https://doi.org/10.5194/essd-2026-94
Preprint. Discussion started: 2 March 2026

uncertainty in detecting authentic climate-driven shifts (Kim et al., 2021; Xie et al., 2025). Beyond these consistency issues, a critical gap remains in data latency. As shown in Table 1, most biophysically consistent records suffer from significant production lags, precluding the inclusion of the near-present period (e.g., up to 2024). Consequently, there is a striking scarcity of datasets that are simultaneously long-term, multi-source consistent, and up-to-date. This vacancy hinders timely assessments of recent climate anomalies, making it difficult to disentangle anthropogenic impacts from natural variability or to monitor emerging extreme events.

The Penman–Monteith–Leuning (PML) model was initially conceived as a high-precision ET diagnostic framework (PML-V1) based on the Penman-Monteith equation coupled with Leuning's canopy conductance theory (Leuning et al., 2008; Zhang et al., 2008), which successfully established a long-term global ET record covering 1982–2012 (Zhang et al., 2016c). Another theoretical advance occurred with the development of the PML-V2 model, a coupled water and carbon flux model that estimates canopy conductance through the GPP process, thereby providing a more physically consistent and high-accuracy estimation of both ET and GPP (Zhang et al., 2019; Gan et al., 2018). Implemented on the Google Earth Engine (GEE) platform (Gorelick et al., 2017), this second generation leveraged the extensive FLUXNET2015 dataset and MODIS data for parameterization to achieve a spatial resolution of 500 m at an 8-day interval, initially covering 2003–2017. Consequently, despite its high accuracy, the original PML-V2 framework lacks a consistent methodology to bridge the gap between AVHRR and MODIS observations, leaving a critical void in our understanding of long-term ecosystem responses and recent climate-driven anomalies.

To provide an integrated, high-fidelity record that resolves the trade-offs between spatial resolution and temporal depth, we introduce the PML-V2.2 dataset. Built upon a robust diagnostic framework, PML-V2.2 extends the coupled record to nearly 43 years (1982–2024). The dataset is strategically released as three complementary products: the “a” version provides 500 m near-present capability based on MODIS; the “b” version utilizes AVHRR to anchor historical estimates essential for climate attribution; and the “c” version systematically integrates their strengths into a continuous, globally consistent record. This design ensures that PML-V2.2 serves as a timely resource, supporting both high-resolution operational monitoring and robust long-term trend analysis in terrestrial hydro-climatic studies. Our new PML-V2.2 datasets have the following features:

1. Consistent forcing data: All simulations (1982–2024) share the same forcing data from bias-corrected MSWEP and MSWX to ensure internally consistent modelling results;
2. Expanded calibration: A significantly larger number of flux-tower sites for model calibration (208 versus 95 used in Zhang et al. (2019));
3. Refined cropland estimates: More accurate ET estimates for croplands that are separated into irrigated and non-irrigated; and
4. Optimized parameterization: The new two-parameter function for vapor pressure deficit is employed, reducing the number of parameters by one compared to the previous version (Zhang et al., 2019; He et al., 2022).

A detailed description of these new features is provided in Sections 2 and 3.

https://doi.org/10.5194/essd-2026-94
Preprint. Discussion started: 2 March 2026

Table 1. Summary of major remote-sensing-driven diagnostic ET and GPP models and datasets.

Dataset Variable	Group	Model / Dataset	Temporal coverage	Temporal resolution	Spatial resolution	Key feature	Reference
ET	Since 2000s	MODIS MOD16	2000-present	8-day	500 m	Penman-Monteith (PM) model incorporating surface resistance and vegetation control	Mu et al. (2011)
		ETMonitor	2000-2021	Daily	1km	Multi-process framework utilizing downscaled soil moisture to separately estimate five distinct ET components	Zheng et al. (2022)
		CoSEB	2000-2020	Daily	500 m	Energy-balanced framework enforcing closure via multivariate random forest	Wang et al. (2025, 2026)
		3T	2001-2020	Daily	0.25°	Parameter-free Three-Temperature model robust under extreme weather conditions	Yu et al. (2022)
	Since 1980s	GLASS	2000-2023/ 1981-2022	8-day	500 m / 0.05°	Multi-algorithm ensemble using Bayesian Model Averaging for robust estimation	Yao et al. (2013, 2014)
		GLEAM4	1980-2024 (near present)	Daily	0.1°	Hybrid framework combining running soil water balance with Machine Learning (ML)-driven water stress	Miralles et al. (2025)
		P-LSHv2	1982-2023	Daily	0.1°	Process-based model with quantile-based soil moisture constraints to reduce uncertainty	Feng et al. (2025)
		SiTHv2	1982-2022	Daily	0.1°	Coupled water-energy scheme synchronizing ET and soil moisture dynamics	Zhang et al. (2024)
		CR	2000-2022/ 1982-2016	Monthly	0.25° / 0.1°	Calibration-free approach grounded in Complementary Relationship (CR) theory	Ma et al. (2021)
		PML-V1	1982-2012	Half-month	0.0833°	PM-based model using Leuning stomatal conductance for water-carbon linkage	Leuning et al. (2008); Zhang et al. (2016c)
GPP	Since 2000s	MODIS MOD17	2000-present	8-day	500 m	Standard Light Use Efficiency (LUE) model constrained by vapor pressure deficit (VPD) and temperature	Running et al. (2004)
		FluxSat	2000-present	Daily	0.05°	Neural network model upscaling eddy covariance tower GPP using MODIS Nadir BRDF-Adjusted Reflectances (NBAR)	Joiner and Yoshida (2020)
		VPM	2000-2016	8-day	500 m / 0.05°	LUE model using Land Surface Water Index (LSWI) to account for moisture stress	Xiao et al. (2004); Zhang et al. (2017)
		GOSIF	2000-2024 (near present)	8-day	0.05°	Upscaled Solar-induced Chlorophyll Fluorescence (SIF)-based GPP tracking actual plant physiological activity	Li and Xiao (2019)
		GloFlux	2000-2023	Monthly	0.1°	ML integration of comprehensive multi-network fluxes to enhance global coverage	Yuan et al. (2025a)
	Since 1980s	GLASS EC-LUE	2000-2024 1981-2018 (near present)	8-day	500 m / 0.05°	LUE framework integrating CO_2 fertilization and VPD-related moisture limits	Yuan et al. (2010); Zheng et al. (2020)
		LRF	1982-2015	Daily	0.05°	Non-linear photosynthesis model employing asymptotic light response function	Tagesson et al. (2021)
		NIRv	1982-2018	Monthly	0.05°	Structure-based proxy using Near-Infrared Reflectance of vegetation (NIRv) to mitigate GPP saturation in dense canopies	Wang et al. (2021)
		BEPS	1981-2019	Daily	0.072°	Process-based two-leaf model applying Farquhar biochemical kinetics	Chen et al. (2019)
ET & GPP	Since 2000s	FLUXCOM-X-BASE	2001-2021	Hourly	0.05°	Advanced ML framework providing hourly fluxes and transpiration consistent with atmospheric constraints	Nelson et al. (2024)
		BEPS-DP	2001-2020	Hourly	0.25°	Hourly process-based simulation with ML-derived dynamic physiological parameters (DP)	Leng et al. (2024)
		PML-V2.0	2003-2017	8-day	500 m	Biophysical coupling of ET and GPP by incorporating carbon assimilation theory	Zhang et al. (2019)
	Since 1980s	BESS V2.0	1982-2022	Daily	0.05°	Integrated water-carbon coupling via two-leaf canopy and enzyme kinetics	Li et al. (2023a)
		PML-V2.2	2000-2024 1982-2024 (near present)	8-day / half-month	500 m / 0.1°	Extended long-term PML dataset with enhanced parameterization using expanded flux data	This study

Note: Datasets with a spatial resolution coarser than 0.25° are excluded from this summary. The literature search and data availability check were concluded on January 25, 2026. Access links for all products are provided in Table A1. In this study, "present" refers to data with a production delay of several days to ~1 month. Due to the latency in meteorological and remote sensing forcing data, "near present" refers to datasets updated through 2024.

https://doi.org/10.5194/essd-2026-94
Preprint. Discussion started: 2 March 2026

2 Methods and materials

2.1 Penman-Monteith-Leuning model

The PML-V2 model partitions terrestrial ET into three constitutive components: vegetation transpiration (E_c), soil evaporation (E_{is}), and canopy interception (E_i) (Zhang et al., 2019). Within a Penman-Monteith (PM) framework, the model utilizes LAI for canopy-soil energy partitioning. Crucially, E_c is estimated through a GPP-coupled canopy conductance (G_c) scheme to ensure biophysical consistency (Gan et al., 2018). E_s is estimated by determining the soil moisture stress by accumulated precipitation and soil equilibrium evaporation (Zhang et al., 2010), while E_i is quantified via the Gash rainfall interception model (van Dijk and Bruijnzeel, 2001).

$$E_c = \frac{\varepsilon A_c + \left(\rho c_p/\gamma\right) D_a\, G_a}{\varepsilon + 1 + G_a/G_c} \tag{1}$$

$$E_s = \frac{f \varepsilon A_s}{\varepsilon + 1} \tag{2}$$

$$E_i = \begin{cases} f_v P & P < P_{wet} \\ f_v P_{wet} + f_{ER}(P - P_{wet}) & P \geq P_{wet} \end{cases} \tag{3}$$

where $\varepsilon = s/\gamma$, in which γ is the psychrometric constant (kPa °C^{-1}) and $s = de^*/dT$ is the slope of the curve relating saturation water vapour pressure to temperature (kPa °C^{-1}). A_c and A_s are the available energy (net absorbed radiation minus soil heat flux, MJ m^{-2} d^{-1}) separated by LAI for E_c and E_s. ρ is the density of air (g m^{-3}). c_p is the specific heat of air at constant pressure (J g^{-1} °C^{-1}). D_a is the water vapour pressure deficit of the air (kPa). G_a is the aerodynamic conductance (m s^{-1}). G_c is the canopy conductance (m s^{-1}). f is a dimensionless variable that determines the water availability for soil evaporation. P is the daily precipitation (mm d^{-1}). P_{wet} is the reference threshold rainfall amount if the canopy is wet (mm d^{-1}). f_{ER} is the ratio of average evaporation rate over average precipitation intensity storms (unitless), f_v is the fractional area covered by intercepting leaves (unitless).

The defining feature of PML-V2 is its coupled water-carbon mechanism. Unlike traditional PM-based models, it derives canopy conductance (G_c) directly from the photosynthesis process, constrained by vapor pressure deficit (D_a). Furthermore, it incorporates the impact of atmospheric CO_2 concentration (C_a) on carbon assimilation and G_c, providing a more physically robust simulation of ET and GPP under changing environmental conditions.

$$GPP = A_{c,g} \cdot f(D_a) \tag{4}$$

$$f(D_a) = \begin{cases} 1, & D_a \leq D_{min} \\ \dfrac{D_{max} - D_a}{D_{max} - D_{min}}, & D_{min} < D_a < D_{max} \\ 0, & D_a \geq D_{max} \end{cases} \tag{5}$$

where $A_{c,g}$ is the gross assimilation rate without D_a constraint. $f(D_a)$ is the D_a constraint function adopted from Wang et al. (2014) and Running et al. (2015).

https://doi.org/10.5194/essd-2026-94
Preprint. Discussion started: 2 March 2026

In this model, the carbon assimilation and water exchange are subject to a unified constraint from D_a. Therefore, a same function $f(D_a)$ can be used for deriving G_c:

$$G_c = 1.6 \cdot m \cdot A_{c,g} \cdot f(D_a)/C_a \tag{6}$$

where m is a dimensionless stomatal conductance coefficient. Note that 1.6 is the ratio of stomatal conductance to water vapor relative to that to carbon flux (Medlyn et al., 2011; Yebra et al., 2013; Gan et al., 2018).

More details on the PML modelling can be found on the supplement of Zhang et al. (2019). Compared with that, the D_0 parameter and the stress function of the original Ball-Berry-Leuning equation are replaced with the two-parameter function. One parameter can be reduced after this update.

2.2 Bottom-up parameterization and validation

The ten parameters of the PML-V2.2 model were optimized and validated using a comprehensive bottom-up framework based on the latest global eddy covariance (EC) flux observations (Table 2). Flux measurements were compiled from six major international monitoring networks including FLUXNET2015 (Ueyama et al., 2025), the Australian and New Zealand flux tower network (OzFlux) (Beringer et al., 2016; Isaac et al., 2017; Beringer et al., 2022), AmeriFlux (Novick et al., 2018; Chu et al., 2023), the Integrated Carbon Observation System (ICOS) (Heiskanen et al., 2022; Warm Winter 2020 Team et al., 2022; Icos Ri et al., 2025), JapanFlux (Ueyama et al., 2025), ChinaFlux (Yu et al., 2006, 2024), and other independent data providers (Liu et al., 2018, 2013b; Ma et al., 2020; Zhou et al., 2023).

For sites with missing data, gap-filling and flux partitioning were performed using the REddyProc R package (Wutzler et al., 2018). This processing pipeline aligns with the FLUXNET2015 protocol (Pastorello et al., 2020), incorporating friction velocity (u*) threshold filtering, Marginal Distribution Sampling (MDS) for gap-filling, and standardized carbon flux partitioning. GPP was calculated as the average of estimates derived from both daytime and nighttime partitioning methods (Reichstein et al., 2005; Lasslop et al., 2010). To ensure temporal continuity, missing meteorological forcing data were supplemented using Multi-Source Weighted-Ensemble Precipitation (MSWEP) V2.8 and Multi-Source Weather (MSWX) Past version (Beck et al., 2019, 2022), which integrate multi-source observations and rescaled European Centre for Medium-Range Weather Forecasts (ECMWF) Reanalysis V5 (ERA5) data. Following a protocol consistent with FLUXNET's use of ERA5-Interim, these seamless daily fields were subsequently used to drive the PML model. Finally, all observations were aggregated into daily, 8-day, and monthly timescales, with a Quality Control (QC) flag assigned to represent the proportion of measured and high-quality gap-filled data. To maintain high data standards, only records with QC > 0.9 were retained for further calibration.

To ensure data reliability, a stringent quality control procedure was also applied to the selected sites, following Zhang et al. (2019). Only sites meeting the following criteria were retained: (i) an energy balance closure ratio exceeding 0.75, (ii) a spatially homogeneous flux footprint within a 500 m radius, and (iii) a continuous observational record longer than one year. After filtering, the final dataset comprised 208 sites (~1,400 site-years for ET), representing a substantial expansion compared to the 95 sites used in earlier version 2.0 (Zhang et al., 2019).

https://doi.org/10.5194/essd-2026-94
Preprint. Discussion started: 2 March 2026

Open Access Earth System Science Data Discussions

Plant functional type (PFT) classifications were harmonized between the International Geosphere–Biosphere Programme (IGBP) and European Space Agency Climate Change Initiative (ESA CCI) schemes, which are intended to be used for the versions "a" and "b", respectively. While IGBP classifications are directly provided by the flux networks as high-accuracy references, the ESA CCI classes were mapped from IGBP categories through a one-to-one correspondence at the selected sites. For the IGBP scheme, model parameters were calibrated for 12 vegetated PFTs using site-level observations (Fig. 1a). During this harmonization process, the four forest classes (ENF, EBF, DNF, and DBF) and other key types, including grasslands (GRA) and croplands (CRO), were mapped to their corresponding ESA CCI classes (e.g., GRASS-NAT and GRASS-MAN) to ensure a perfect match (Fig. 1b). To ensure robust cross-validation, the nine open and closed shrublands (CSH / OSH) were merged into a single shrubland (SH / SHRUBS) class. Furthermore, the 30-m 2015 Landsat-derived Global Rainfed and Irrigated-cropland Product (LGRIP) (Teluguntla et al., 2023) was used to further split CRO and GRASS-MAN into rainfed (RFD) and irrigated (IRR) types. Finally, all vegetated PFTs were parameterized with EC data, while the four non-vegetated classes (water, ice, barren land, and urban areas) were assigned static values.

Consequently, we retained a subset of 172 sites (82.7% of the 208 IGBP sites) that exhibited perfect one-to-one alignment between IGBP and CCI classification, enabling both schemes to share identical parameter sets (Table 2). This rigorous selection was necessary because initial investigations revealed that some ESA CCI labels did not align with the strict physical definitions of the classes. Specifically, the 36 sites where mixed forests (MF) were labeled as specific forest types, or where woody savannas (SAV), savannas (SAV), and wetlands (WET) were labeled as grasslands, were excluded to ensure classification integrity. During modelling, the CCI classification uses fractions of other PFTs to interpret these IGBP PFTs.

Model calibration was conducted independently for each PFT, and cross-validation was performed using a leave-one-out strategy within each PFT (Zhang et al., 2019 and He et al., 2022). This means that for each PFT, the parameters were optimized using all sites except one, and the calibrated model was then used to predict the omitted site. This process was iterated so that each site, in turn, was left out for prediction, ensuring that all sites within a PFT were ultimately predicted. Compared to version 2.0, PML-V2.2 employs an enhanced multi-objective error metric (F) (Viney et al., 2009; Zhang et al., 2016b), which places a heightened emphasis on bias control to improve simulation accuracy:

$$\mathrm{F} = 2 - (\mathrm{NSE}_{\mathrm{ET}} + \mathrm{NSE}_{\mathrm{GPP}}) + 5|\ln(1 + \mathrm{Bias}_{\mathrm{ET}})|^{2.5} + 5|\ln(1 + \mathrm{Bias}_{\mathrm{GPP}})|^{2.5} \tag{7}$$

$$\mathrm{NSE} = 1 - \frac{\sum_{i=1}^{n}\left|y_{sim,i} - y_{obs,i}\right|^2}{\sum_{i=1}^{n}\left|y_{obs,i} - \overline{y_{obs}}\right|^2} \tag{8}$$

$$\mathrm{Bias} = \frac{\sum_{i=1}^{n} y_{sim,i} - \sum_{i=1}^{n} y_{obs,i}}{\sum_{i=1}^{n} y_{obs,i}} \tag{9}$$

where NSE is the Nash–Sutcliffe efficiency of the 8-day ET or GPP. Bias is the model bias. $y_{obs,i}$ and $y_{sim,i}$ are the observed and simulated values at time step i. $\overline{y_{obs}}$ is the mean of all observations.

This objective function jointly optimizes the NSE and Bias for both ET and GPP. By simultaneously constraining temporal dynamics (via NSE) and long-term water and carbon balance (via Bias), this formulation improves the robustness and transferability of model parameters for global-scale applications.

https://doi.org/10.5194/essd-2026-94
Preprint. Discussion started: 2 March 2026

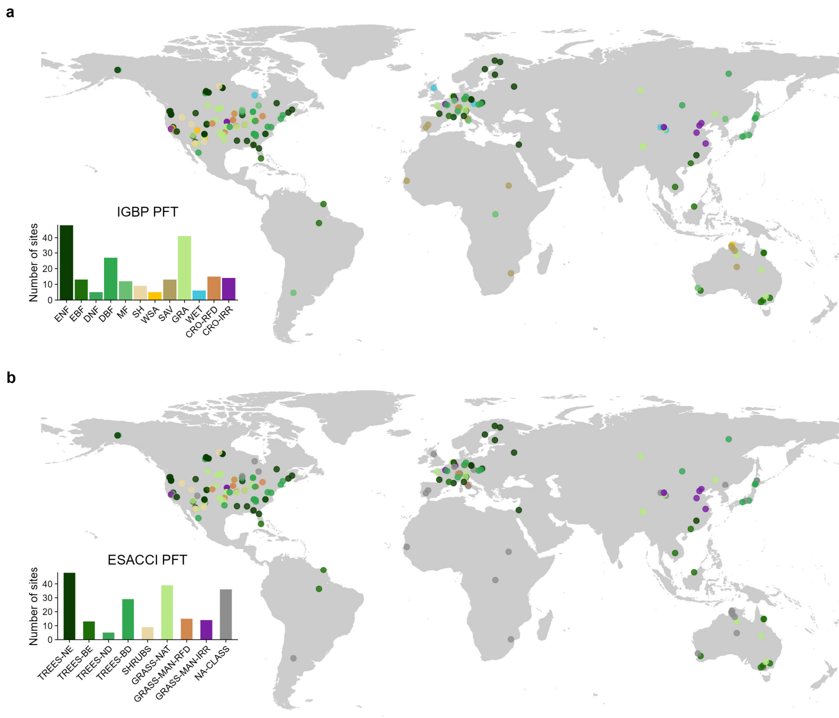

Figure 1. Global distribution of eddy covariance flux towers for model calibration and validation.

Table 2. Optimized PML-V2.2 model parameters for the harmonized IGBP and CCI PFTs

IGBP PFT[a]	CCI PFT	β	η	V_m	k_Q	k_A	D_{min}	D_{max}	m	S_l	F_0
ENF	TREES-NE	0.031	0.027	10.8	0.60	0.60	0.65	3.50	3.7	0.09	0.08
EBF	TREES-BE	0.030	0.020	10.4	0.59	0.51	0.65	3.51	4.9	0.10	0.05
DNF	TREES-ND	0.037	0.021	11.1	0.41	0.52	0.71	3.56	3.2	0.07	0.09
DBF	TREES-BD	0.031	0.020	10.0	0.57	0.90	0.65	3.50	4.1	0.12	0.09
MF	/	0.030	0.021	10.5	0.58	0.77	0.66	4.10	4.1	0.12	0.11
OSH/CSH[b]	SHRUBS[c]	0.030	0.065	25.9	0.49	0.89	1.00	4.14	3.3	0.09	0.11
WSA	/	0.045	0.022	12.2	0.50	0.89	1.06	3.74	3.3	0.12	0.10
SAV	/	0.030	0.024	14.3	0.60	0.88	0.69	5.17	3.5	0.12	0.09
GRA	GRASS-NAT	0.031	0.044	12.1	0.59	0.87	1.07	3.76	2.9	0.12	0.06
WET	/	0.030	0.023	11.0	0.58	0.87	0.92	5.39	8.4	0.05	0.06
CRO-IRR[d]	GRASS-MAN-IRR	0.040	0.069	22.9	0.40	0.90	1.16	3.54	4.3	0.10	0.06
CRO-RFD	GRASS-MAN-RFD	0.033	0.061	14.2	0.45	0.71	0.76	4.54	2.9	0.11	0.12

[a]IGBP PFT are reported by data suppliers of the flux network. [b]Due to limited number of shrub sites for robust model calibration, the open shrublands and closed shrublands are combined. [c]ESA CCI PFT has four types of SHRUBS (NE, BE, ND, BD), which are also combined. [d]Croplands are splitted as rainfed (RFD) and irrigated (IRR) types based on the IGRIP30 dataset. The corresponding human-managed grass (GRASS-MAN) class is also splitted. Note that β *is* initial slope of the light response curve to assimilation rate (i.e. quantum efficiency), η is initial slope of the CO_2 response curve to assimilation rate (i.e. carboxylation efficiency), V_m is maximum catalytic capacity of Rubisco per unit leaf area at 25 °C. k_Q is extinction

https://doi.org/10.5194/essd-2026-94
Preprint. Discussion started: 2 March 2026

coefficient of PAR. k_A is extinction coefficient of available energy. $D_{\min}$ and $D_{\max}$ are thresholds below which there is no vapor pressure constraint and highest constraint, respectively. m is stomatal conductance coefficient. S_l is specific canopy rainfall storage capacity per unit leaf area. F_0 is specific ratio of average evaporation rate over average rainfall intensity during storms per unit canopy cover.

2.3 Model versions and consolidation

To meet diverse research needs ranging from high-resolution monitoring to long-term climate attribution, this study develops three primary versions of the PML-V2.2 model. PML-V2.2a and PML-V2.2b serve as the foundational products, respectively optimized for the MODIS and AVHRR satellite eras. These versions provide the basis for the final consolidated dataset, PML-V2.2c, which offers a seamless global record from 1982 to the near-present. While the core physics of the PML-V2.2 model remain consistent across all versions, they are distinguished by their specific satellite sensors, spatial resolutions, and Plant Functional Type (PFT) inputs to ensure maximum utility across different spatiotemporal scales (Fig. 2).

A critical enhancement in this framework is the adoption of MSWEP V2.8 and MSWX-Past as meteorological forcing (Beck et al., 2019, 2022), replacing the Global Land Data Assimilation System (GLDAS) V2.1 used in previous versions. The primary driver for this transition was the temporal limitation of GLDAS V2.1, which is restricted to the post-2000 era. In contrast, MSWEP and MSWX offer a seamless, high-accuracy record from 1982 to 2024, enabling the consistent detection of decadal eco-hydrological trends. Beyond temporal coverage, these datasets utilize a unique multi-source fusion strategy that optimally combines gauge, satellite, and reanalysis data. Unlike purely model-based products, this integration significantly reduces biases in precipitation and meteorological variables, providing a climatic baseline with superior accuracy. Furthermore, the native 0.1° resolution of MSWEP/MSWX minimizes the footprint mismatch caused by the coarser 0.25° GLDAS, ensuring better spatial alignment with satellite-derived inputs. For implementation, all forcing variables (e.g., precipitation, radiation, temperature, vapor pressure, wind speed) were spatially aligned using bilinear interpolation (Fig. 2). Additionally, the global monthly atmospheric CO_2 concentration (C_a) data were sourced from the National Oceanic and Atmospheric Administration (NOAA). With these consistent climate forcing and parameter sets, the three datasets are produced as follows.

PML-V2.2a is the MODIS-based version of the framework, providing high-resolution (500 m, 8-day) outputs from 2000 to near present. These MODIS Collection 6.1 inputs include MOD15A2H LAI, MOD43A3 albedo, MOD11A2 emissivity, and MOD12Q1 IGBP PFT data (Myneni et al., 2021; Schaaf and Wang, 2021; Wan et al., 2021; Friedl and Sulla-Menashe, 2022). While it maintains consistency with the physical structure of earlier versions, PML-V2.2a incorporates the latest model parameters calibrated against an expanded dataset of 208 flux tower sites. A key technical advancement is the integration of the V0.1.6 LAI smoothing algorithm (Kong et al., 2019). This upgraded version enhances outlier detection and specifically avoids the common pitfall of over-smoothing. Consequently, it accurately preserves the signals of bimodal seasonality in double-cropping croplands and mitigates the chronic underestimation of LAI in tropical regions caused by frequent cloud cover and rainfall (He et al., 2022). These refinements contribute to a theoretically higher accuracy and better representation of vegetation heterogeneity.

https://doi.org/10.5194/essd-2026-94
Preprint. Discussion started: 2 March 2026

PML-V2.2b is the AVHRR-based version designed for historical eco-hydrological analysis, providing half-month 0.1° outputs from 1982 to 2020. This version utilizes the GIMMS LAI4g dataset (Cao et al., 2023; Zhu et al., 2013) as its primary vegetation input. Unlike its predecessors, GIMMS LAI4g employs a deep-learning-based consolidation strategy that effectively eliminates satellite orbital drift and sensor degradation, ensuring consistency across the pre- and post-2000 eras. For model parameterization, these vegetation dynamics are paired with GLASS albedo and emissivity products (Liu et al., 2013a; Cheng et al., 2016; Liang et al., 2021) and ESA CCI PFT data (Harper et al., 2023). To match the model grid, the high-resolution land cover data were aggregated to 0.1° resolution by calculating the fractional coverage of five major PFTs within each grid. Although restricted by the coarser spatial resolution of AVHRR compared to MODIS, PML-V2.2b provides the necessary decadal continuity for studying terrestrial water and carbon cycles over the past 39 years. By employing the same climate forcing, model and parameters as version "a", it ensures that the foundational diagnostic mechanisms remain consistent across different satellite epochs.

PML-V2.2c is the final consolidated dataset (half-month 0.1°) generated through a rigorous, pixel-scale bi-directional consolidation between the AVHRR- and MODIS-based versions from 1982 to near present. Using the 2001–2003 overlapping period as a reference (Fig. 2b), we treated version "a" as the primary benchmark, which is aggregated to half-month 0.1° resolution. For most pixels, the primary variables of version "b" were scaled to match the mean values of version "a" to ensure statistical alignment. In extreme scenarios, such as desert regions or instances where version "a" detected vegetation (>0) but version "b" remained at zero (preventing standard scaling), a reverse scaling or masking to zero was applied to maintain absolute consistency. This harmonization effectively eliminates systematic "jumps" caused by sensor transitions and PFT classification differences, ensuring that the 43-year record preserves both accurate mean states and genuine long-term trends.

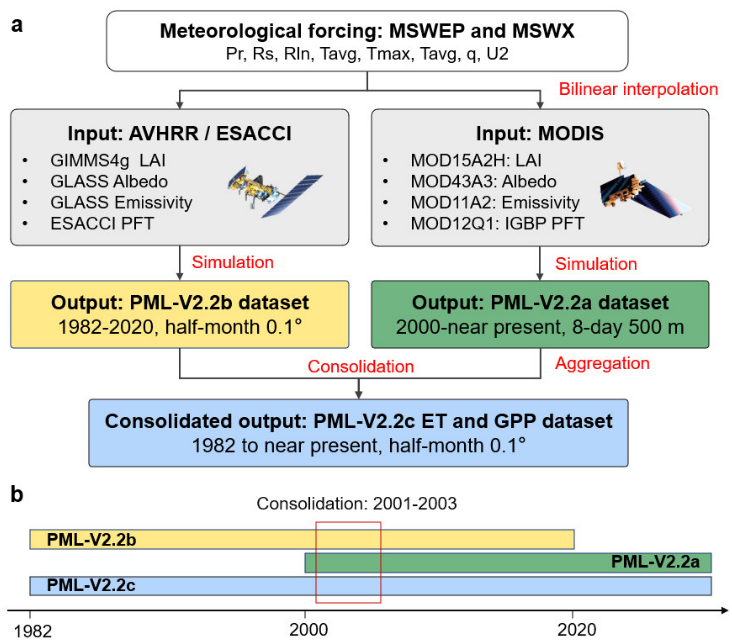

Figure 2. Dataset versions and consolidation.

https://doi.org/10.5194/essd-2026-94
Preprint. Discussion started: 2 March 2026

2.4 Top-down water balance validation

We use top-down water balance ET (ET_{WB}) estimates to independently validate our new PML ET estimates. At the annual scale, water balance ET is estimated by solving the basin-scale water balance equation using precipitation (P), streamflow (Q), and changes in terrestrial water storage (dS/dt):

$$ET_{WB} = P - Q - dS/dt \tag{10}$$

To account for inherent uncertainties in individual components of the water balance, the validation integrates multiple observation-based data sources. Similar to Ma et al. (2024), precipitation is obtained from several widely used products, including the MSWEP V2.8 (Beck et al., 2019), the Global Precipitation Climatology Project (GPCP) V3.3 (Huffman, 2024), the Global Precipitation Climatology Centre dataset (GPCC) version 2022 (Schneider et al., 2022), and the Climatic Research Unit Time Series (CRU-TS) V4.09 (Harris et al., 2020). Streamflow data are compiled from in situ observations provided by the Global Runoff Data Centre (GRDC), the United States Geological Survey (USGS), and the Australian Bureau of Meteorology (BoM-AU). Changes in terrestrial water storage (dS/dt) are derived from Gravity Recovery and Climate Experiment and its Follow-On mission (GRACE/FO), including solutions from the Jet Propulsion Laboratory (JPL) (Save et al., 2016; Save, 2022), the Center for Space Research (CSR) (Watkins et al., 2015; Wiese et al., 2016, 2018), and the Goddard Space Flight Center (GSFC) (Loomis et al., 2019) during 2003-2020, as well as from the GRACE reconstruction dataset (GRACE-REC) (Humphrey and Gudmundsson, 2019) during 1982-2016. dS/dt is computed as a mean of the differences between consecutive Januarys and Decembers at an annual scale.

By combining these independent data sources, the analysis explicitly accounts for observational uncertainties, which can vary substantially across regions. Basin-scale water-balance ET estimates (ET_{WB}) are obtained using a Bayesian three-cornered hat method, which allows for the estimation of a consensus ET signal while minimizing the influence of individual data-source errors. The associated uncertainty (σ) is quantified as the standard deviation across all feasible combinations of Pr, Q, and dS/dt datasets.

$$\sigma_{ET} = \sqrt{{\sigma_P}^2 + {\sigma_Q}^2 + {\sigma_{dS/dt}}^2} \tag{11}$$

where σ are computed as standard deviation among different data sources and processing methods. Following Ma et al. (2024), a relative uncertainty of 5% is assumed for Q.

This validation framework is applied across multiple spatial and temporal scales. Specifically, it includes an analysis of more than 56 large river basins (Ma et al., 2024), covering approximately 29% of the global land surface for the period 1982-2016, and an expanded assessment of over 152 large basins, representing about 42% of global land area, for the period 2003-2020 (streamflow data extended from Zhang et al. (2023)).

https://doi.org/10.5194/essd-2026-94
Preprint. Discussion started: 2 March 2026

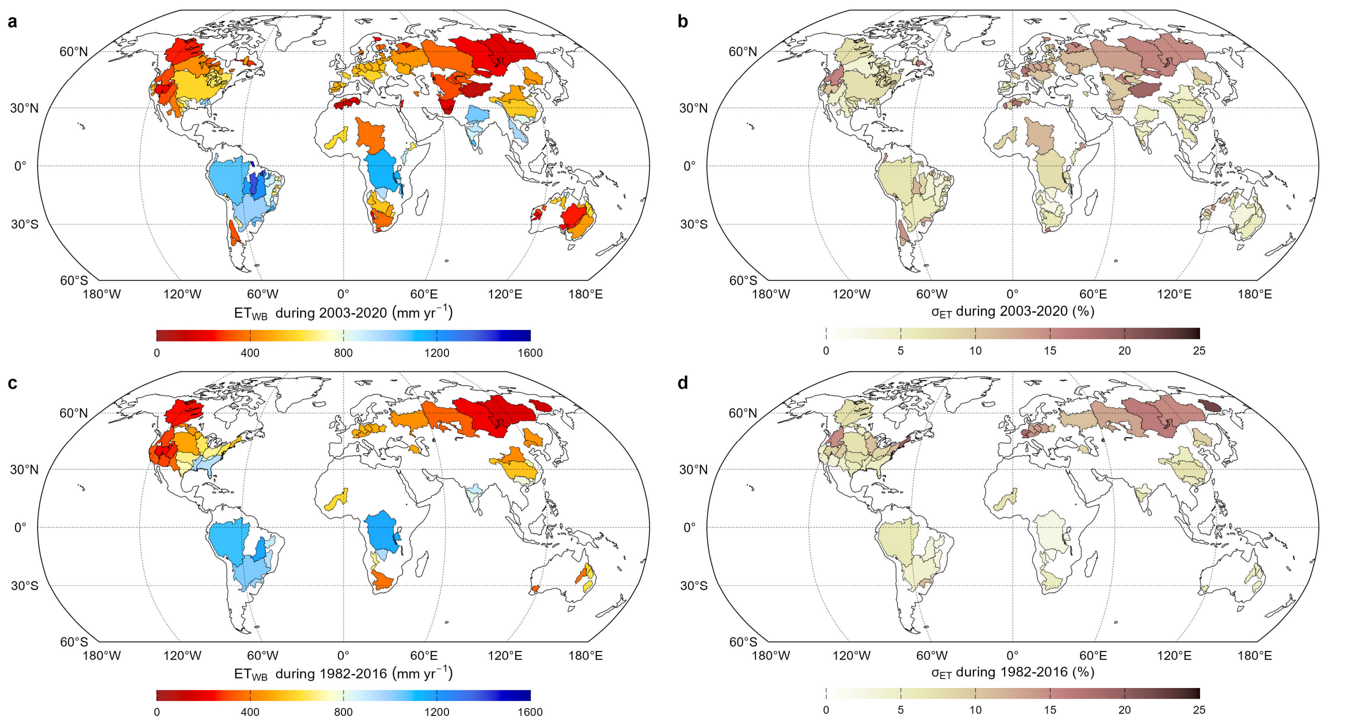

Figure 3. Multi-source water balance ET and its associated uncertainty.

2.5 Statistical analysis

The predictive accuracy of the model is evaluated using a suite of performance metrics, including NSE, Bias, the correlation coefficient (R), and Root Mean Square Error (RMSE). These metrics are selected to provide a balanced assessment, as they compensate for each other's specific limitations. While R measures the strength of the linear relationship and NSE evaluates the overall fit relative to the observed mean, both can be sensitive to extreme outliers or peak flows. To address this, RMSE is used to quantify the absolute error in the same units as the data, and Bias is employed to detect any systematic over- or under-estimation (volume error). Together, this multi-metric approach ensures that the model is validated for its ability to capture both the timing and the magnitude of the observed data.

To interpret long-term changes, the non-parametric Mann-Kendall (MK) test and Sen's Slope estimator are applied to quantify the significance and magnitude of trends. These methods are robust against outliers and non-normal distributions, ensuring that the results represent long-term trends rather than impact of anomalies.

https://doi.org/10.5194/essd-2026-94
Preprint. Discussion started: 2 March 2026

3 Results

3.1 Model calibration and validation

The PML model demonstrates high proficiency in estimating 8-day ET and GPP across the 208 eddy covariance sites (Fig. 4). Overall, the model performs robustly in capturing flux variability, indicated by ET statistical metrics: NSE = 0.72, R = 0.86, RMSE = 0.64 mm d^{-1}, Bias = −1.7%, and GPP statistical metrics: NSE = 0.76, R = 0.87, RMSE = 1.97 g C m^{-2} d^{-1}, Bias = 0.2%. Similarly, it has robust model performance in cross-validation for both ET and GPP, with only slight degradation in overall NSE and other metrics. The validation of WUE (GPP per unit of ET consumption) at the site scale demonstrates robust model performance across both multi-year and annual scales, with cross-validation NSE values of 0.515 and 0.348, respectively, and absolute biases consistently maintained within 5% (Fig. A1). The clustering of points along the 1:1 line across both calibration and validation phases demonstrates the model's robustness in capturing flux variability across diverse site conditions.

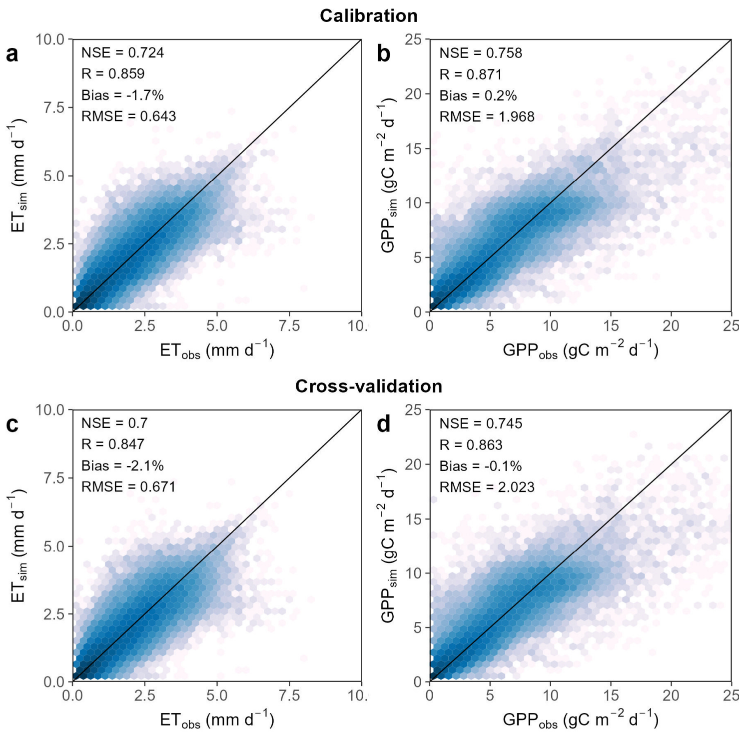

Figure 4. Model calibration and cross-validation result under IGBP classification of the total 208 sites.

Building upon these global site-level assessments, the model's performance remains highly stable when analyzed across different PFTs (Fig. 5). For ET performance, accuracy is consistent across most biomes, with PFT-specific NSE values typically ranging from 0.45 to 0.78 and R values between 0.74 and 0.92. PFTs such as grassland (GRA), deciduous

https://doi.org/10.5194/essd-2026-94
Preprint. Discussion started: 2 March 2026

broadleaf forest (DBF), and wetlands (WET) exhibit the highest precision in water flux estimation, with RMSE generally staying between 0.5 and 0.95 mm d^{-1}. Bias is limited to within ±5% for the majority of categories.

Regarding GPP performance, the model achieves even higher metrics across the PFT spectrum, with NSE reaching up to 0.88 and R values exceeding 0.90 for types like WET and deciduous needleleaf forest (DNF). While agricultural types—specifically irrigated (CRO-IRR) and rainfed (CRO-RFD) croplands—display higher absolute errors (RMSE) compared to natural vegetation, their biases remain tightly clustered around zero. This indicates that the model effectively captures the magnitude of carbon productivity with minimal systematic error across different vegetation structures.

Overall, the model demonstrates exceptional robustness and regionalization capability, with high consistency between calibration and cross-validation metrics across biomes. This robustness is particularly evident in GPP estimates, which show greater stability than ET during validation. Despite this reliability, some PFT-specific sensitivities persist: EBF remains challenging to simulate due to low seasonal variability limiting the signal-to-noise ratio, while DNF shows a sharper cross-validation drop in ET NSE likely due to limited representation (only four sites). Nonetheless, the high consistency across most PFTs confirms the model's reliability for capturing complex eco-hydrological processes under varying conditions.

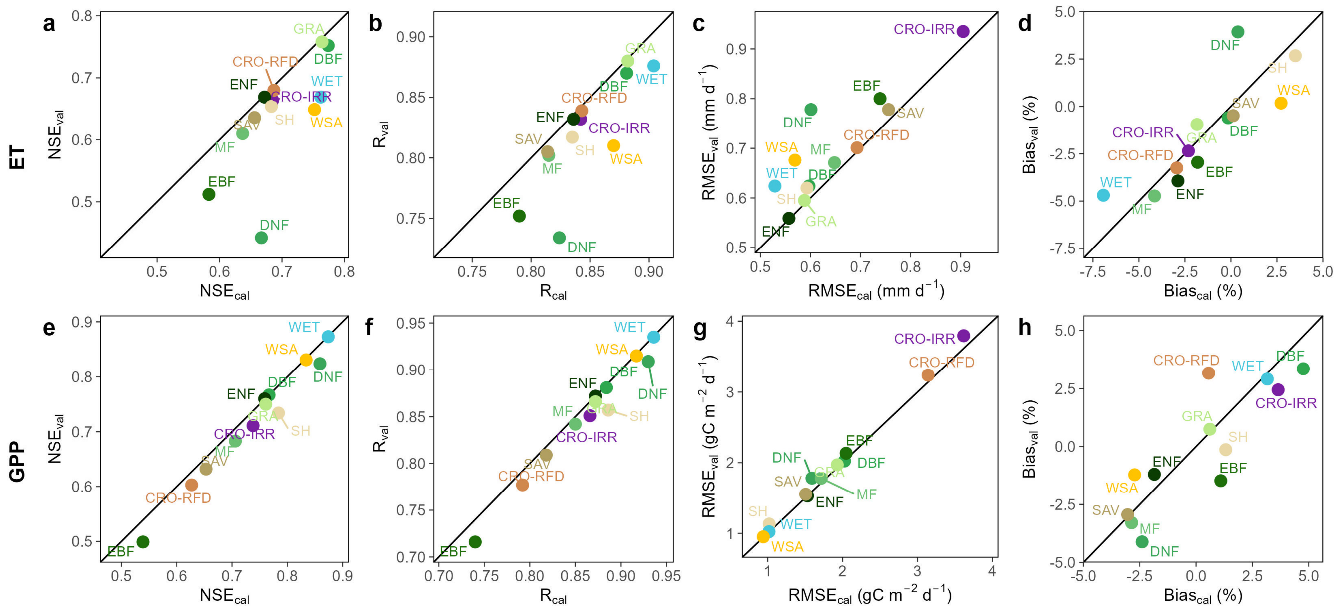

Figure 5. Calibration and cross-validation result over different PFTs under IGBP classification. Note that 8 of the 12 IGBP PFTs have the same parameters but with different names under CCI classification (Table 2).

https://doi.org/10.5194/essd-2026-94
Preprint. Discussion started: 2 March 2026

3.2 Improved parameterization of croplands

The implementation of a splitted parameterization scheme for rainfed (CRO-RFD) and irrigated (CRO-IRR) croplands led to significant performance improvements (Fig. 6). For rainfed systems, the model showed a notable increase in the NSE by 0.07 and a reduction in RMSE by 0.07 mm d^{-1}, effectively mitigating systematic biases with a decrease in ET Bias of 10.04%. While the irrigated ET precision metrics remained relatively stable, the Bias shifted by +7.37% toward the zero-baseline, suggesting a more accurate representation of water availability and management in irrigated agricultural lands compared to the traditional mixed approach.

Substantial enhancements were also observed in GPP simulations, where the splitted scheme addressed systematic errors more effectively than the mixed model. GPP RMSE decreased by 0.17 and 0.24 g C m^{-2} d^{-1} for RFD and IRR, while Bias was dramatically improved by 18.85% and 13.58%. Overall, this parameterization scheme reduced the magnitude of systematic errors across all agricultural lands by an average of 8.7% for ET and 16.2% for GPP. This suggests that the conceptual simplification of treating irrigated and rainfed crops as distinct entities enables a more physically consistent representation of agricultural cycles. By separately capturing high-productivity irrigated regimes and moisture-limited rainfed growth, this approach effectively achieves a better closure of both water and carbon balances.

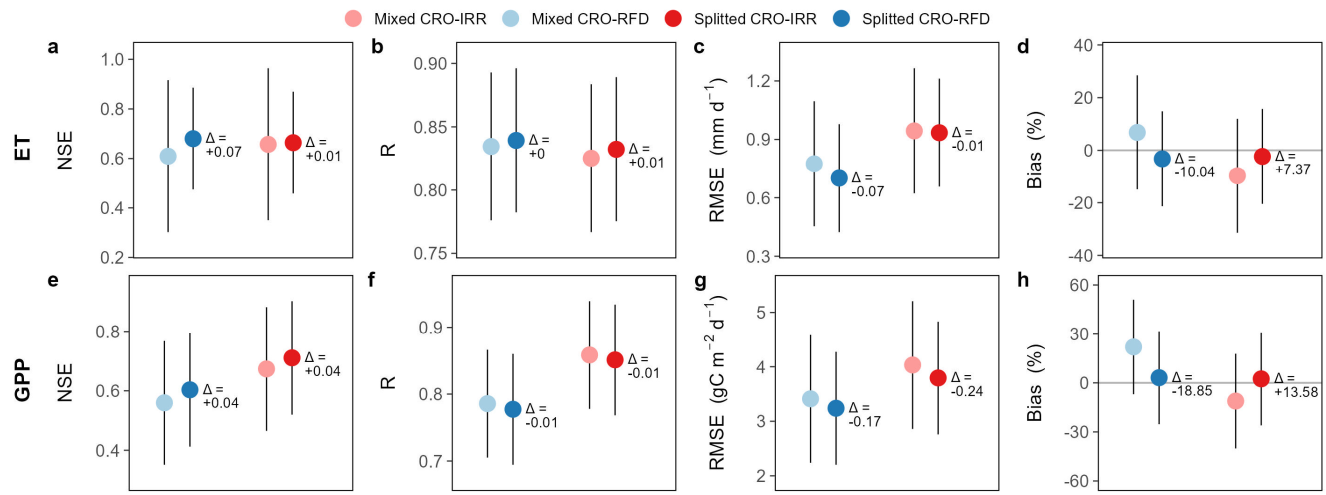

Figure 6. Improvement in cross-validation by splitted parameterization over rainfed and irrigated croplands compared with mixed parameterization. The evaluation was conducted across 29 flux sites, including 14 irrigated and 15 rainfed sites.

3.3 Basin-scale water balance validation

Basin-scale validation against water-balance-derived ET (ET_{WB}) confirms the robust performance of all three PML-V2.2 products across different historical periods (Fig. 7). Across both the 2003–2020 (152 basins) and 1982–2016 (56 basins) evaluation windows, the products consistently yield high accuracy with NSE values of 0.89–0.91 and R ≥ 0.95. Subtle

https://doi.org/10.5194/essd-2026-94
Preprint. Discussion started: 2 March 2026

discrepancies exist between versions "a" and "b", primarily driven by differences in LAI, albedo, and PFT inputs. While the point-wise statistics indicate a slight underestimation for most products, the primary biases for all versions remain well within ±6%. Notably, supplementary analysis (Fig. A2) reveals a marginal bias when results are aggregated by basin area, highlighting the relative effects inherent in basin-scale water balance validation. While ET_{WB} estimates are not entirely bias-free (Fig. 3), the validation results remain within a reasonable and acceptable range, particularly given the robust NSE values across basins.

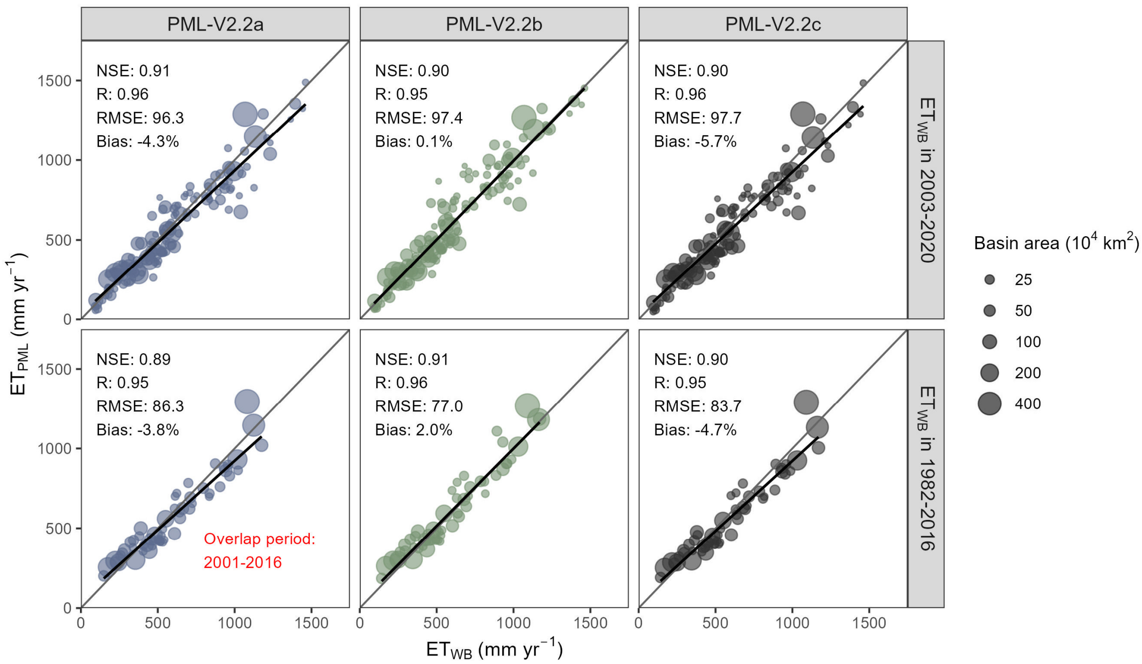

Figure 7. Comparison of simulated ET from three versions of PML-V2.2 datasets with water-balance-derived ET (ET_{WB}) averaged for two basin datasets over different historical periods (1982–2016 and 2003–2020). Note that ET_{WB} data are shown in Fig. 3. The four evaluation metrics here are computed without area weights, while an additional figure considering area weights are shown in Fig. A2.

3.4 Consistency of consolidation

To evaluate the consistency and reliability of the data integration process, the decadal trends of the AVHRR-based product (PML-V2.2b) were compared against the previous version (PML-V2.2a) for the overlapping period 2001–2020 (Fig. 8). The annual anomalies exhibit excellent agreement, with high consistency for ET (NSE = 0.90) and GPP (NSE = 0.79), indicating that the reconstructed dataset robustly captures interannual hydro-climatic fluctuations. The decadal trends of both ET and GPP also show a high degree of consistency across the global land surface. For ET, the two versions exhibit a strong correlation (R = 0.92) and a high NSE = 0.83 (slightly lower than NSE = 0.904 of ET anomalies due to uncertainty in trend estimation). Similarly, GPP trends demonstrate significant agreement with an R value of 0.81 and an NSE of 0.64. These statistical results are further corroborated by the spatially coherent global patterns shown in Fig. A3. While slight regional variations exist due to remote-sensing forcing data inputs, the overall alignment along the 1:1 line confirms that the consolidation process preserves the core long-term hydro-climatic signals of the original datasets.

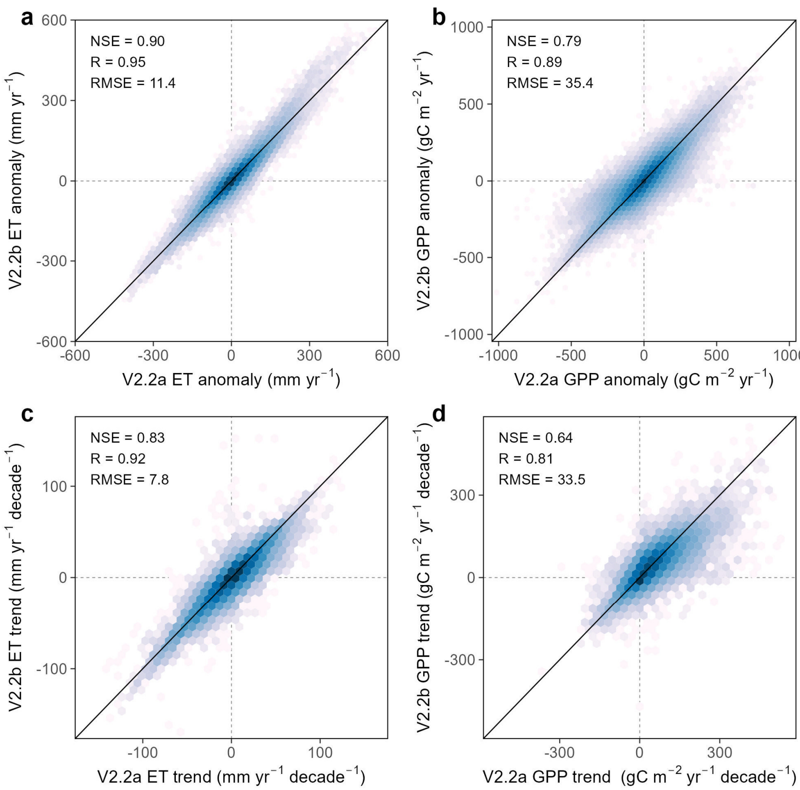

Figure 8. Consistency of interannual variability and decadal trends between AVHRR-based PML-V2.2b and MODIS-based PML-V2.2a during the overlapping period of 2001–2020. Panels a and b compare the annual anomalies for ET and GPP, respectively, indicating the agreement in interannual variability. Panels c and d compare the decadal trends (see Fig. A3 for the corresponding spatial trend maps). The metrics are calculated based on aggregated grids at a 0.5° resolution to demonstrate the robustness of the consolidation process.

3.5 Global patterns and trends during 1982–2024

The global spatial distribution of long-term mean ET during 1982–2024 exhibits strong latitudinal gradients, reflecting the fundamental role of energy and water availability (Fig. 9). The highest ET fluxes, exceeding 1000 mm yr^{-1}, are concentrated in tropical rainforests across the Amazon Basin, Congo Basin, and Southeast Asia. In these humid regions, vegetation transpiration and interception loss are the primary contributors to the total water flux. Conversely, ET values remain minimal in arid and semi-arid regions such as the Sahara and Central Australia, where water limitation severely constrains surface

https://doi.org/10.5194/essd-2026-94
Preprint. Discussion started: 2 March 2026

evaporation. The PML-V2.2 product effectively captures these hydro-climatic constraints, showing that transpiration dominates the global ET budget over most vegetated land surfaces. Overall, the PML-V2.2c product estimates global ET of 65.8 × 10^3 km^3 yr^{-1} during 1982–2024. This corresponds to a mean flux of 509 mm yr^{-1} averaged over a land area of 1.292 × 10^8 km^2 (excluding inland water bodies, permanent snow and glaciers). The partitioning reveals that 58.0%, 30.4%, and 11.6% of this flux are contributed by transpiration, soil evaporation, and interception evaporation, respectively.

Terrestrial productivity and its coupling with water consumption are characterized by the spatial distributions of GPP and WUE (Fig. 10). The global total GPP in the PML-V2.2c dataset is approximately 143.0 PgC yr^{-1}, peaking in tropical biomes (above 2,500 gC m^{-2} yr^{-1}), where photosynthesis is maximized by abundant sunlight and moisture. However, the WUE pattern reveals a different ecological strategy: the highest WUE values are found in temperate forests and certain semi-arid shrublands, indicating high carbon assimilation per unit of water lost. These spatial patterns highlight the regional differences in how ecosystems balance their carbon-water trade-offs, with the PML-V2.2 dataset providing a consistent representation of these global productivity gradients.

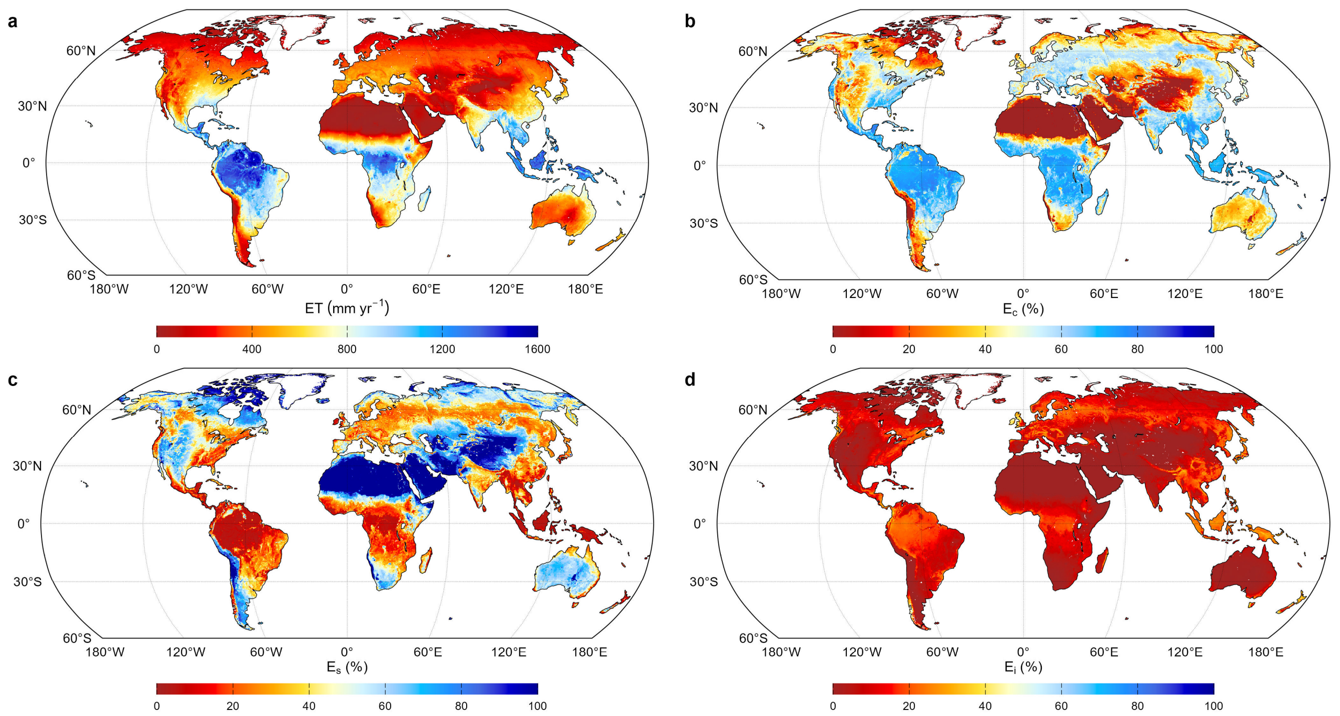

Figure 9. Global patterns of terrestrial evapotranspiration (ET) and its components of the PML-V2.2c dataset during 1982–2024.

https://doi.org/10.5194/essd-2026-94
Preprint. Discussion started: 2 March 2026

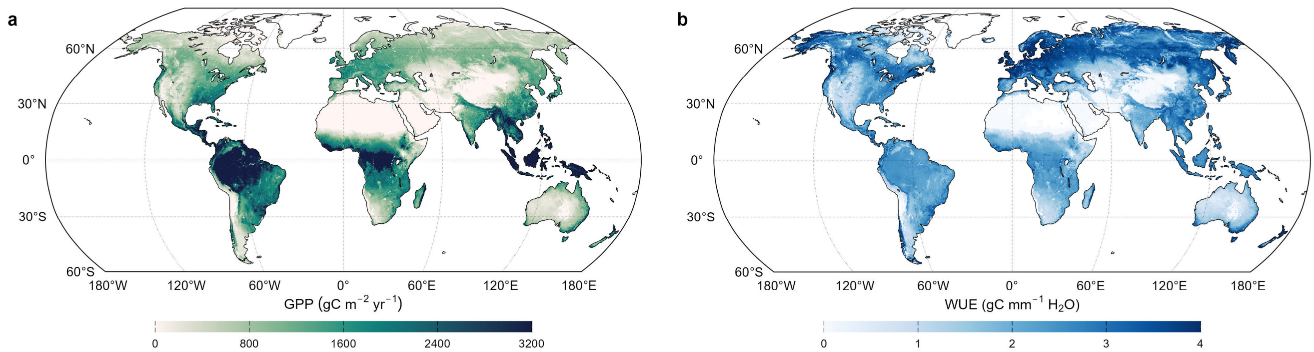

Figure 10. Global patterns of terrestrial gross primary production (GPP) and water use efficiency (WUE) of the PML-V2.2c dataset during 1982–2024. WUE is computed by GPP / ET.

The long-term dynamics from 1982 to 2024 reveal an intensifying global water and carbon cycle, characterized by widespread increasing trends (Fig. 11 & Fig. A4). Global GPP has shown a robust and significant increase (α = 0.315 PgC yr^{-2}, $p < 0.01$), particularly in greening hotspots like China, India, and Europe. Parallel to carbon gains, global ET also exhibits a significant upward trend ($\alpha = 0.019 \times 10^3$ km^3 yr^{-2}, $p < 0.01$), primarily driven by the increasing transpiration and interception. While most regions show positive trajectories, notable regional heterogeneity exists, with declining ET trends in parts of the western US, South America and Southern Africa. Overall, the global-scale consistent rise in GPP, ET, and WUE (Fig. A4) underscores the significant impact of CO_2 fertilization and climate change on terrestrial ecosystem functions over the past 43 years.

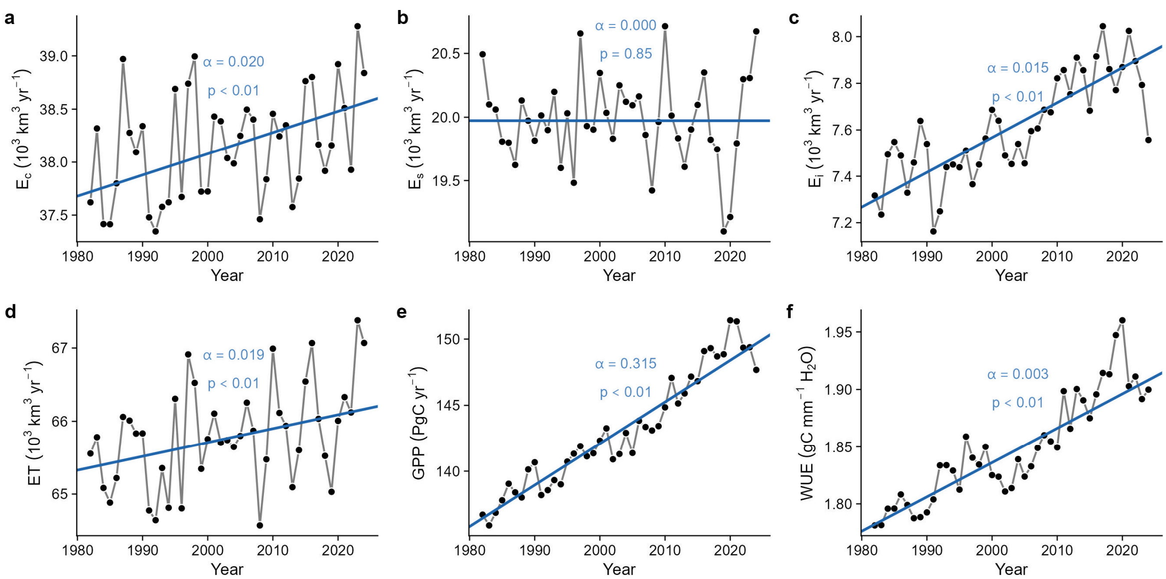

Figure 11. Interannual variations and long-term trends of global water and carbon fluxes of the PML-V2.2c dataset during 1982–2024. Panels a–d represent the global annual sums (10^3 km^3 yr^{-1}) of E_c, Es, Ei, and total ET. Panels e–f show the global

https://doi.org/10.5194/essd-2026-94
Preprint. Discussion started: 2 March 2026

area-weighted sum of GPP (PgC yr^{-1}) and mean of WUE (gC mm^{-1} H_2O), respectively. All global calculations exclude water bodies to focus on terrestrial surfaces. The blue solid lines indicate the linear trends, where α denotes the Sen's Slope estimates (10^3 km^3 yr^{-2}, PgC yr^{-2}, or gC mm^{-1} H_2O yr^{-1} for different variables) and the p-value represents the significance level determined by the MK test.

4 Discussion

The transition to the PML-V2.2 series represents a significant advancement in model stability and accuracy. By implementing a refined optimization framework and updated PFT schemes, the absolute bias is mostly within 5% across diverse biomes, a stark contrast to previous versions where ET bias could reach 10% and GPP bias could be more than 25% during cross-validation (Fig. 5 in Zhang et al. (2019)). A critical improvement is observed in cropland simulations. While remote sensing-based LAI partially captures the reduced water limitation in agricultural areas, our results suggest that differences in stomatal conductance are another factor in determining accuracy. By incorporating two basic irrigation types into the parameterization, the model better reflects the enhanced productivity of managed lands. Despite these gains, substantial potential remains for further refinement. Future iterations should focus on moving beyond static PFT-based parameters toward a scheme that integrates dynamic vegetation attributes, such as leaf traits and hydraulic properties, directly into the parameterization framework to better capture physiological responses to environmental change (Yan et al., 2025).

The temporal consistency of the PML-V2.2 product from 1982 to 2024 (as seen in Fig. 12) demonstrates its robustness for long-term climate studies. This stability is primarily attributed to the use of unified meteorological forcing and parameter sets across different satellite eras. While the consolidated inputs (specifically GIMMS LAI4g and GLASS albedo) may inevitably contain residual uncertainties (Cao et al., 2023), the resulting global and regional coherence remains remarkably high (Fig. 8 & Fig. A3). Looking forward, this framework is well-positioned to integrate Visible Infrared Imaging Radiometer Suite (VIIRS) data, which serves as the operational successor to the aging MODIS sensors (Yan et al., 2021; Endsley et al., 2025). These results suggest that, under the current model structure, PML-V2 can be continuously updated to provide a reliable, long-term record for critical assessments, such as the State of Global Water Resources Report compiled by World Meteorological Organization (2025), where high-fidelity, multi-decadal data are required to monitor global hydro-climatic shifts.

Differences in global means between the current and earlier PML versions are likely driven by the shift from GLDAS 2.1 to MSWEP/MSWX climate forcing (Kim et al., 2021; Xie et al., 2025), alongside updated parameterization, updated LAI data and smoothing algorithms. In version 2.0, the model predicted an aggressive increase in ET and GPP during 2003-2010 but followed by sharp declines. Our analysis reveals that these spurious trends may result from the high volatility in the solar radiation terms of the GLDAS forcing used in that version. Comparatively, the new global mean GPP and WUE exhibit a continuing upward trend, a more physically plausible result in a greening world. Overall, while both versions have similar

https://doi.org/10.5194/essd-2026-94
Preprint. Discussion started: 2 March 2026

range of global patterns and total fluxes, the new version is recommended for users as it covers a longer period and offers higher quality as validated from eddy flux observations and water balance.

Our global ET estimate of 65.8×10^3 km^3 yr^{-1} during 1982–2024 is slightly lower than recent estimates by Zhang et al. (2026). In their updated assessment of global water cycle variables, they report a mean annual land ET of $69.0 \pm 6.2 \times 10^3$ km^3 yr^{-1} for 1981–2014, excluding Greenland and Antarctica. Our estimate also excludes these regions, but additionally omits evaporation from surface inland water bodies, which is approximately $1.5 \pm 0.15 \times 10^3$ km^3 yr^{-1} (Zhao et al., 2022a). When this water body evaporation is included, our adjusted global ET becomes very similar to or 2.5% less than the mean value reported by Zhang et al. (2026). Our updated parameter sets differ from the PML V2.0 version (Zhang et al., 2019) due to three key refinements: (i) an expanded calibration using 208 global flux sites from the original 95 sites for improved robustness; (ii) a new distinction between irrigated and rainfed croplands that reduced their internal ET biases by 8.7%; and (iii) the removal of a parameter to enhance model parsimony without losing accuracy. Compared to 12 mainstream diagnostic models during basin-scale water balance validation (Fig. A5 and Fig. A6), the PML models consistently demonstrate top-tier performance, ranking as the best or second-best among all products evaluated. Specifically, PML achieves the highest NSE (0.89-0.91) and the lowest RMSE (77.0 to 96.3 mm yr^{-1}).

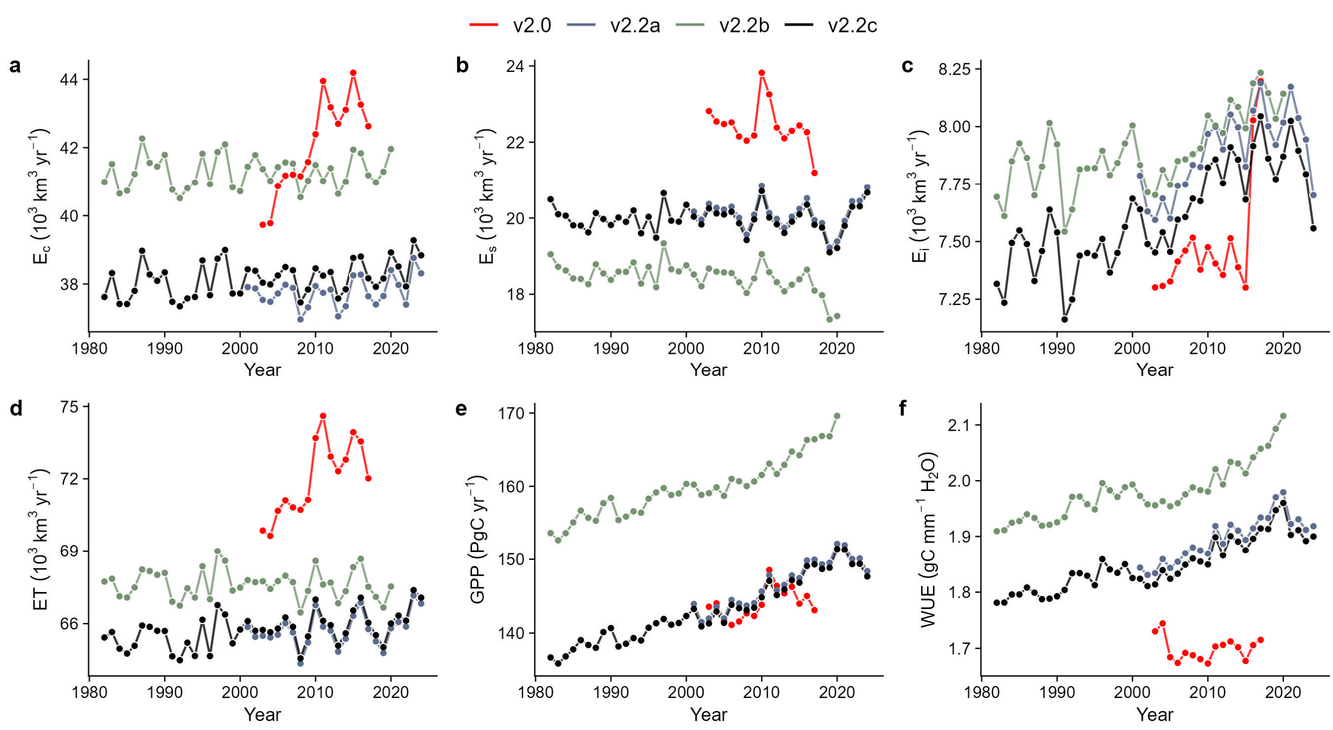

Figure 12. Comparison of interannual variations and long-term trends in global water and carbon fluxes across different PML-V2 versions.

https://doi.org/10.5194/essd-2026-94
Preprint. Discussion started: 2 March 2026

Our global GPP estimate of 143.0 PgC yr^{-1} during 1982–2024 is in closer alignment with the evolving consensus in the carbon cycle community. Traditional satellite optical remote sensing-driven products, specifically LUE-based upscaling (~115 PgC yr^{-1}), machine learning-based upscaling (~124 PgC yr^{-1}), and process models (~131 PgC yr^{-1}), tend to converge within a lower range. Our result is significantly higher but aligns more closely with contemporary estimates derived from novel proxies and ensemble assessments, such as the soil respiration constraints (~149 ± 25 PgC yr^{-1}), the ^{18}O signature of atmospheric CO_2 (150–175 PgC yr^{-1}), and the latest carbonyl sulfide (OCS)-based results by Lai et al. (2024) (157 ± 8.5 PgC yr^{-1}). Crucially, the robust biophysical coupling of ET and GPP within the PML model, supported by extensive global flux tower parameterization, ensures a more physically consistent and reasonable simulation of the water-carbon cycle.

The long-term trends of PML-V2.2c offer a nuanced view of the global water cycle, showing a more conservative ET growth of approximately +1.25% during 1982–2024. In terms of linear trends, our estimate of 0.24 mm yr^{-2} during 1982–2011 is significantly more moderate compared to the ensemble mean of six diagnostic products (0.66 ± 0.38 mm yr^{-2}) (Yang et al., 2023). Similarly, when benchmarked against a broader ensemble of 11 ET products (1982–2016) with a median trend of 0.28 mm yr^{-2} (Ma et al., 2021), our estimate of 0.18 mm yr^{-2} for the same period remains on the lower end of the spectrum. This global trajectory results from the offsetting dynamics of internal components. The observed marginal increase in transpiration is likely driven by the interplay between structural greening and physiological CO_2 effects. Specifically, the reduction in stomatal conductance and water demand induced by rising CO_2 largely offsets the structural effect of increased leaf area (Zhang et al., 2021; Wei et al., 2024; Lesk et al., 2025; Wei et al., 2025). Simultaneously, interception evaporation shows a significant upward trend following LAI increases, while soil evaporation has slightly decreased due to the reduced available energy at the soil surface caused by canopy shading. The magnitude of global GPP remains consistent with other independent data sources (Yang et al., 2022; Lai et al., 2024; Wang et al., 2024), reflecting a strong increase in WUE due to greening. While uncertainties remain, the internal consistency of the PML-V2 framework makes these results a valuable tool for multi-model assessments and climate attribution research, providing a stable benchmark for understanding how the terrestrial biosphere regulates water and carbon fluxes.

5 Data availability

The original PML-V2.2a dataset at 8-day 500 m resolution (2000–2024) is freely accessible via Google Earth Engine at https://developers.google.com/earth-engine/datasets/catalog/projects_pml_evapotranspiration_PML_OUTPUT_PML_V22a. The aggregated 0.1° version of PML-V2.2a (2000-2024), along with the PML-V2.2b (1982–2020) and PML-V2.2c (1982–2024) datasets, are available at the National Tibetan Plateau Data Center (TPDC) under https://doi.org/10.11888/Terre.tpdc.303314 (Xu et al., 2026).

https://doi.org/10.5194/essd-2026-94
Preprint. Discussion started: 2 March 2026

6 Conclusion

The development of PML-V2.2 establishes an internally consistent, 43-year (1982–2024) record of the global terrestrial water and carbon cycles. The high statistical and spatial agreement between the MODIS-based (V2.2a) and AVHRR-based (V2.2b) products validates the multi-tier architecture, ensuring that the consolidated PML-V2.2c dataset provides a reliable multi-decadal benchmark for climate attribution. By leveraging an expanded calibration of 208 flux sites and distinguishing between irrigated and rainfed systems, the dataset achieves exceptional fidelity, yielding global mean ET and GPP estimates of 65.8×10^3 km^3 yr^{-1} (with 58.0% from transpiration) and 143.0 PgC yr^{-1}, respectively. The successful top-down water-balance validation (NSE = 0.89–0.91) across 152 large basins during 2003–2020 and 56 basins during 1982–2016 further confirms that this framework provides a physically plausible representation of global eco-hydrological states.

Beyond data production, this long-term record offers critical insights into the intensifying global water-carbon cycle. Specifically, global GPP has significantly increased at a rate of 0.315 PgC yr^{-2} during 1982–2024 ($p < 0.01$), while global ET exhibits a significant but more constrained rise of 0.019×10^3 km^3 yr^{-2} ($p < 0.01$). This trend underscores a complex interplay of feedback mechanisms: while global greening increases structural water demand through expanded leaf area, this is largely counteracted by the physiological water-saving effects of rising atmospheric CO_2.

Looking ahead, the stability demonstrated during the sensor transition period ensures that the PML-V2.2 framework can be reliably extended into the VIIRS era as MODIS reaches its end-of-life. The data fusion and bias-correction strategies employed here provide a robust template for maintaining multidecadal continuity in the face of sensor degradation. Future scientific refinements will focus on transitioning from static, PFT-based parameters toward dynamic schemes that integrate functional vegetation traits, such as leaf nitrogen and hydraulic properties, to better capture physiological responses to escalating climate extremes. As an evolving and high-accuracy record, PML-V2.2 is positioned to support critical international assessments, such as the WMO State of Global Water Resources reports, providing the foundational data continuity required for climate adaptation, trend attribution, and global water management.

https://doi.org/10.5194/essd-2026-94
Preprint. Discussion started: 2 March 2026

Open Access Earth System Science Data Discussions

Appendices: Supplementary tables and figures

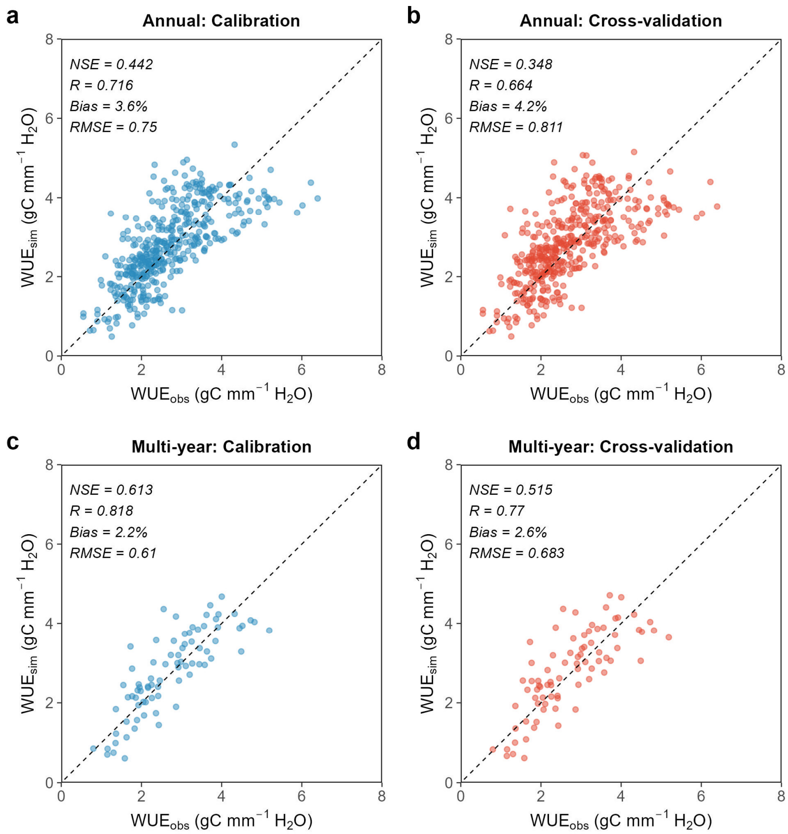

Figure A1. Calibration and cross-validation of WUE at annual scale. Annual WUE is derived from ET and GPP averages
515 with >80% 8-day availability, while multi-year WUE necessitates at least five years of valid data.

https://doi.org/10.5194/essd-2026-94
Preprint. Discussion started: 2 March 2026

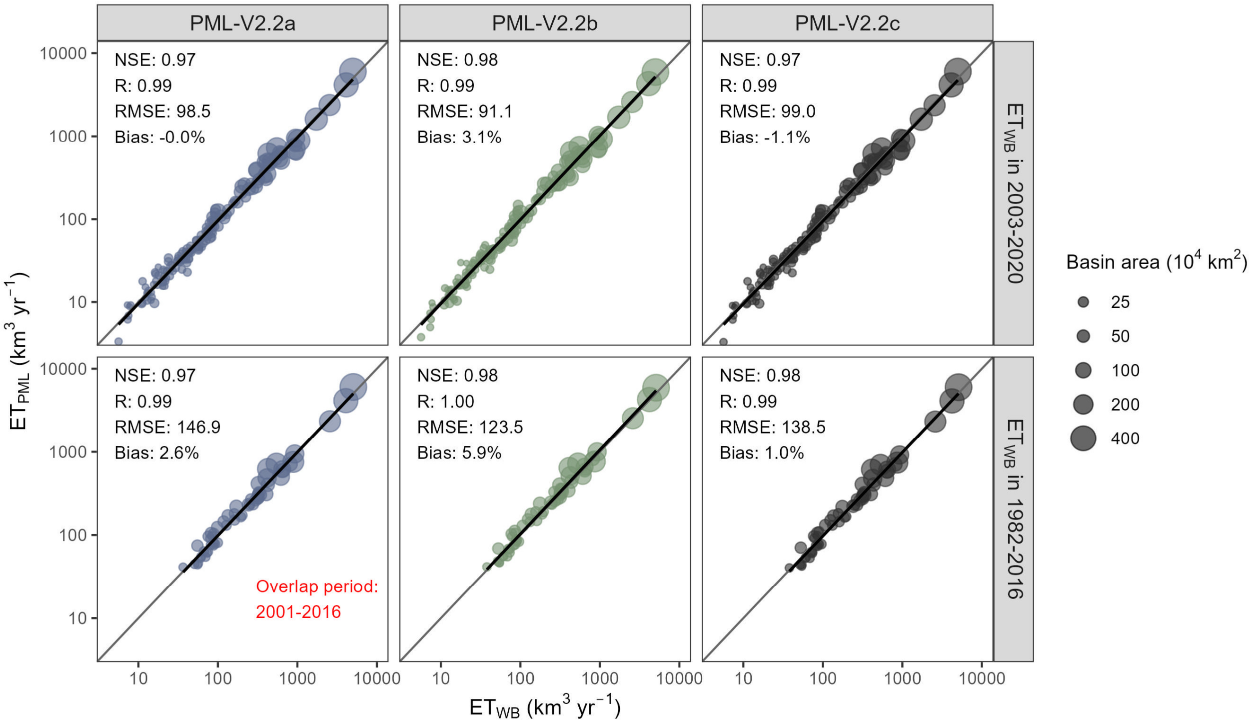

Figure A2. Comparison of simulated ET with water-balance-derived ET averaged for two basin datasets over different historical periods (1982–2016 and 2003–2020). Note that compared with Figure 7, ET considers basin area coverage and is expressed as km^3 year^{-1}.

https://doi.org/10.5194/essd-2026-94
Preprint. Discussion started: 2 March 2026

Open Access Earth System Science Data Discussions

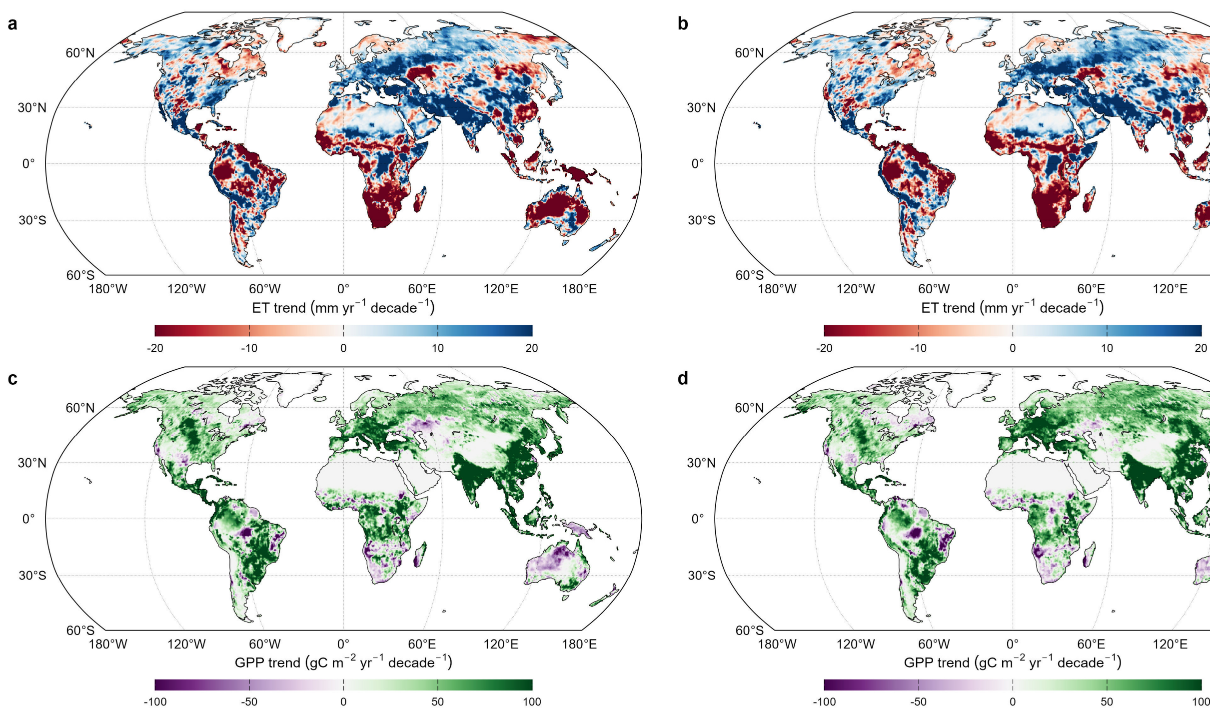

Figure A3. Spatial consistency of ET and GPP trends between the baseline PML-V2.2a and the consolidated PML-V2.2b during the overlapping period (2001–2020). Panels (a) and (b) show the spatial distribution of ET trends from V2.2a and V2.2b, respectively. Panels (c) and (d) show the comparison for GPP trends. The highly similar spatial patterns verify that PML-V2.2b successfully captures the climate-driven trends observed in the MODIS-based PML-V2.2a. Scatter plots of trends at grid scale are provided in Figure 8.

https://doi.org/10.5194/essd-2026-94
Preprint. Discussion started: 2 March 2026

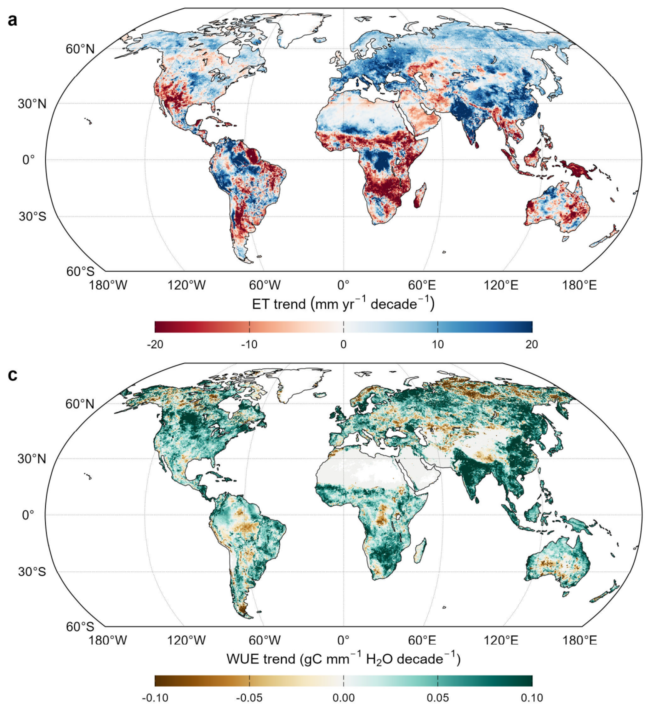

Figure A4. Global trends in ET, GPP, and WUE during 1982–2024 from the consolidated PML-V2.2c dataset.

https://doi.org/10.5194/essd-2026-94
Preprint. Discussion started: 2 March 2026

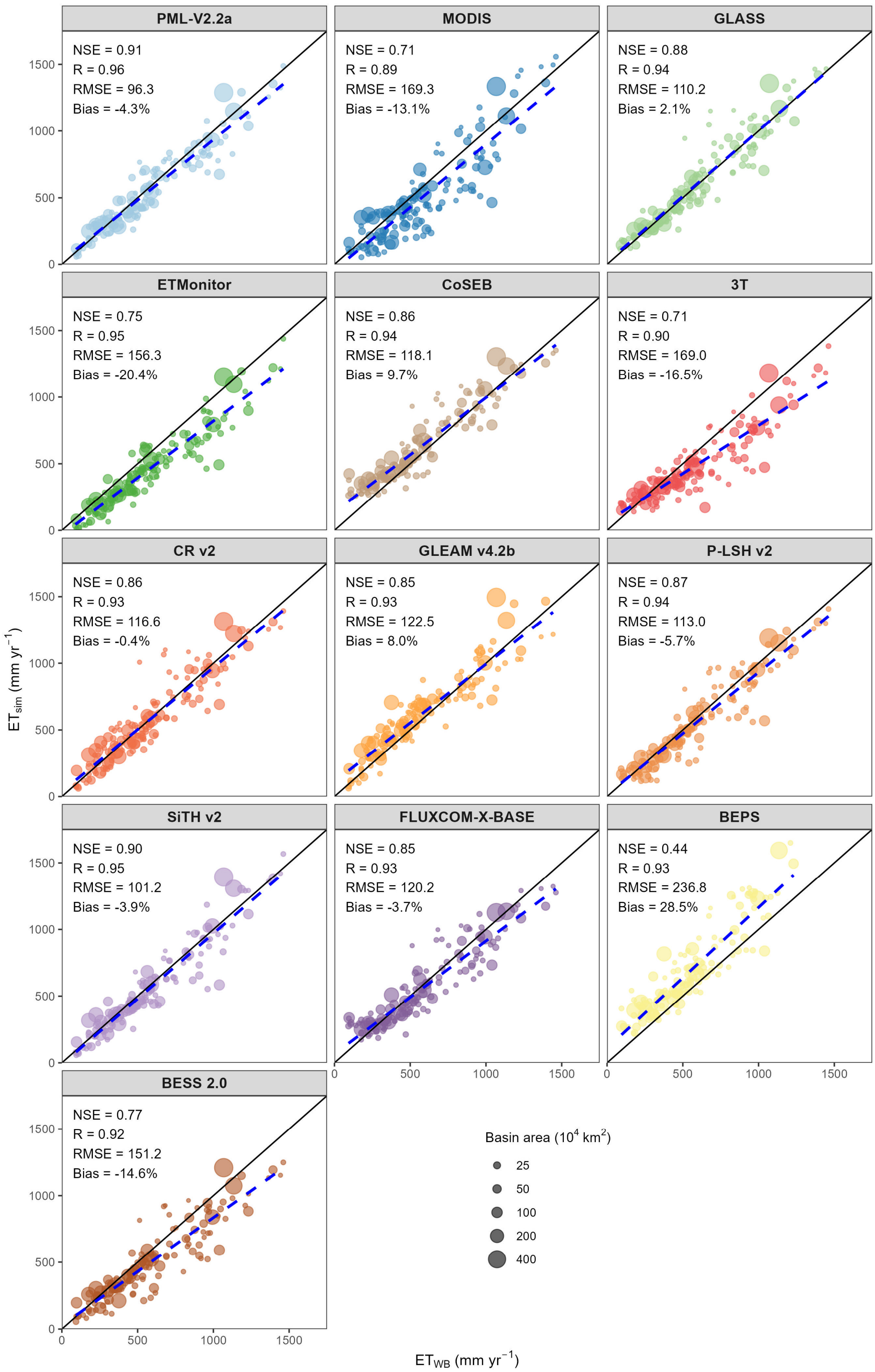

Figure A5. Comparison of simulated ET with water-balance-derived ET averaged for 152 large basins over 2003–2020.

https://doi.org/10.5194/essd-2026-94
Preprint. Discussion started: 2 March 2026

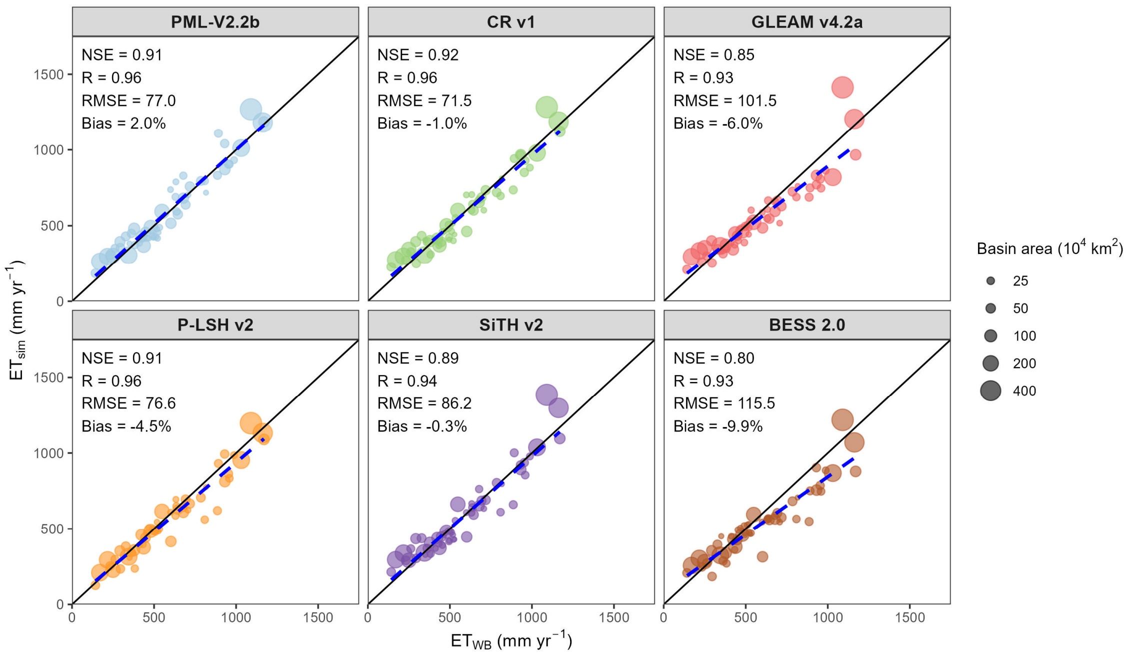

535 **Figure A6.** Comparison of simulated ET with water-balance-derived ET averaged for 56 large basins over 1982–2016.

https://doi.org/10.5194/essd-2026-94
Preprint. Discussion started: 2 March 2026

Earth System Science Data
Open Access Discussions

Table A1. Data links of summarised diagnostic products in Table 1

Dataset Variable	Group	Model / Dataset	Temporal coverage	Temporal resolution	Spatial resolution	Reference	Data link
ET	Since 2000s	MODIS MOD16	2000-present	8-day	500 m	Mu et al. (2011)	https://developers.google.com/earth-engine/datasets/catalog/MODIS_061_MOD16A2
		ETMonitor	2000-2021	Daily	1km	Zheng et al. (2022)	https://data.tpdc.ac.cn/en/data/c284bd88-7694-4577-9cbb-02684bd940ff
		CoSEB	2000-2020	4-day	500 m	Wang et al. (2025, 2026)	https://doi.org/10.57760/sciencedb.27228
		3T	2001-2020	Daily	0.25°	Yu et al. (2022)	https://doi.org/10.57760/sciencedb.o00014.00001
	Since 1980s	GLASS	2000-2023 / 1981-2022	8-day	500 m / 0.05°	Yao et al. (2013, 2014)	https://glass.hku.hk/archive/ET/
		GLEAM4	1980-2024	Daily	0.1°	Miralles et al. (2025)	https://www.gleam.eu/
		P-LSHv2	1982-2023	Daily	0.1°	Feng et al. (2025)	https://data.tpdc.ac.cn/en/data/a63aaf57-dd15-4a38-8735-12b465bc4cdc
		SiTHv2	1982-2022	Daily	0.1°	Zhang et al. (2024)	https://data.tpdc.ac.cn/en/data/bc51e1b0-494c-4cd5-ae4d-eba6b9d2322c
		CR	2000-2022 / 1982–2016	Monthly	0.25° / 0.1°	Ma et al. (2021)	v1:https://doi.org/10.6084/m9.figshare.22362385; v2: https://doi.org/10.6084/m9.figshare.13634552
		PML-V1	1982-2012	Half-month	0.0833°	Leuning et al. (2008); Zhang et al. (2016c)	https://data.csiro.au/collection/csiro:17375
GPP	Since 2000s	MODIS MOD17	2000-present	8-day	500 m	Running et al. (2004)	https://developers.google.com/earth-engine/datasets/catalog/MODIS_061_MOD17A2H
		FluxSat	2000-present	Daily	0.05°	Joiner and Yoshida (2020)	https://www.earthdata.nasa.gov/data/catalog/ges-disc-fluxsatmgpp-l3-daily-p05deg-2.2
		VPM	2000-2016	8-day	500 m / 0.05°	Xiao et al. (2004); Zhang et al. (2017)	https://doi.pangaea.de/10.1594/PANGAEA.879560
		GOSIF-GPP	2000-2024	8-day	0.05°	Li and Xiao (2019)	https://globalecology.unh.edu/data/GOSIF-GPP.html
		GloFlux	2000-2023	Monthly	0.1°	Yuan et al. (2025a)	https://doi.org/10.11888/Terre.tpdc.301870
	Since 1980s	GLASS EC-LUE	2000-2024 1981-2018 (near present)	8-day	500 m / 0.05°	Yuan et al. (2010); Zheng et al. (2020)	https://glass.hku.hk/archive/GPP/
		LRF	1982-2015	Daily	0.05°	Tagesson et al. (2021)	https://doi.org/10.17894/ucph.b2d7ebfb-c69c-4c97-bee7-562edde5ce66
		NIRv	1982-2018	Monthly	0.05°	Wang et al. (2021)	https://doi.org/10.6084/m9.figshare.12981977
		BEPS	1981-2019	Daily	0.072°	Chen et al. (2019)	https://doi.org/10.12199/nesdc.ecodb.2016YFA0600200.02.00
ET & GPP	Since 2000s	FLUXCOM-X-BASE	2001-2021	Hourly	0.05°	Nelson et al. (2024)	https://meta.icos-cp.eu/collections/_I85vWiIV81AifoxCkty50YI
		BEPS	2001-2020	Hourly	0.25°	Leng et al. (2024)	https://doi.org/10.57760/sciencedb.ecodb.00163
		PML-V2.0	2003-2017	8-day	500 m	Zhang et al. (2019)	https://doi.org/10.11888/Geogra.tpdc.270251 (aggregated 0.05° data)
	Since 1980s	BESS V2.0	1982-2022	Daily	0.05°	Li et al. (2023a)	https://drive.google.com/drive/folders/1i03DkZ0vV3pAnrhSrUYmcxmUtQqMILDs
		PML-V2.2	2000-2024 1982-2024 (near present)	8-day / half-month	500 m / 0.1°	This study	See Data Availability statement in Section 5

https://doi.org/10.5194/essd-2026-94
Preprint. Discussion started: 2 March 2026

Supplement link

The link to the supplement will be included by Copernicus, if applicable.

Author contributions

YZ conceived this study. ZX led material preparation, model simulation, and data analysis. ZX and YZ wrote the first version of the paper. DK provided ongoing data and programming support for model simulations. NM compiled long-term streamflow data and contributed to the water balance analysis. XZ provided expert guidance based on previous AVHRR data versions. All authors contributed to the discussion, interpretation of the results, and writing of the paper.

Competing interests

The authors declare that they have no competing interests.

Disclaimer

Copernicus Publications remains neutral with regard to jurisdictional claims made in the text, published maps, institutional affiliations, or any other geographical representation in this paper. While Copernicus Publications makes every effort to include appropriate place names, the final responsibility lies with the authors. Views expressed in the text are those of the authors and do not necessarily reflect the views of the publisher.

Acknowledgements

We gratefully acknowledge the individuals involved in infrastructure maintenance, field collection, and data processing. Special thanks are due to the following data providers: FLUXNET2015, AmeriFlux, OzFlux, JapanFlux, and ChinaFlux for eddy flux observations; the MSWEP and MSWX team for climate forcing datasets; the CRU, GPCC, GPCP, and MSWEP teams for precipitation (Pr) datasets; the JPL, CSR, and GSFC teams for GRACE/FO and the GRACE-REC team for TWSA datasets; and the GRDC, USGS, BOM, and MWR for streamflow datasets. We also acknowledge the Google Earth Engine platform for providing the cloud computing infrastructure essential for the large-scale data processing and interactive visualization in this study. In particular, we thank Simon Ilyushchenko from Google for his valuable assistance with the data catalog update process. Furthermore, we are grateful to Congcong Li, Xian Wang, Shaoyang He, Xiaojie Li, Yuxuan Xie, Wenjie Hou, Jiangmeng Li, and Lingxiao Huang for their assistance with data preparation, collection, and model simulations.

Financial support

YZ acknowledges financial support from the National Natural Science Foundation of China (Grant No. 42330506 and 42361144709) and the Talent Program of the Ministry of Science and Technology of China. ZX acknowledges financial support from the Postdoctoral Fellowship Program (Grant No. GZC20250236) and General Program (Grant No. 2025M770359) of the China Postdoctoral Science Foundation.

Review statement

The review statement will be added by Copernicus Publications listing the handling editor as well as all contributing referees according to their status anonymous or identified.

References

Beck, H. E., Wood, E. F., Pan, M., Fisher, C. K., Miralles, D. G., Dijk, A. I. J. M. van, McVicar, T. R., and Adler, R. F.: MSWEP V2 global 3-hourly 0.1° precipitation: methodology and quantitative assessment, Bulletin of the American Meteorological Society, 100, 473–500, https://doi.org/10.1175/BAMS-D-17-0138.1, 2019.

Beck, H. E., Dijk, A. I. J. M. van, Larraondo, P. R., McVicar, T. R., Pan, M., Dutra, E., and Miralles, D. G.: MSWX: Global 3-Hourly 0.1° Bias-Corrected Meteorological Data Including Near-Real-Time Updates and Forecast Ensembles, Bulletin of the American Meteorological Society, 103, E710–E732, https://doi.org/10.1175/BAMS-D-21-0145.1, 2022.

Beringer, J., Hutley, L. B., McHugh, I., Arndt, S. K., Campbell, D., Cleugh, H. A., Cleverly, J., Resco de Dios, V., Eamus, D., Evans, B., Ewenz, C., Grace, P., Griebel, A., Haverd, V., Hinko-Najera, N., Huete, A., Isaac, P., Kanniah, K., Leuning, R., Liddell, M. J., Macfarlane, C., Meyer, W., Moore, C., Pendall, E., Phillips, A., Phillips, R. L., Prober, S. M., Restrepo-Coupe, N., Rutledge, S., Schroder, I., Silberstein, R., Southall, P., Yee, M. S., Tapper, N. J., van Gorsel, E., Vote, C., Walker, J., and Wardlaw, T.: An introduction to the Australian and New Zealand flux tower network – OzFlux, Biogeosciences, 13, 5895–5916, https://doi.org/10.5194/bg-13-5895-2016, 2016.

Beringer, J., Moore, C. E., Cleverly, J., Campbell, D. I., Cleugh, H., De Kauwe, M. G., Kirschbaum, M. U. F., Griebel, A., Grover, S., Huete, A., Hutley, L. B., Laubach, J., Van Niel, T., Arndt, S. K., Bennett, A. C., Cernusak, L. A., Eamus, D., Ewenz, C. M., Goodrich, J. P., Jiang, M., Hinko-Najera, N., Isaac, P., Hobeichi, S., Knauer, J., Koerber, G. R., Liddell, M., Ma, X., Macfarlane, C., McHugh, I. D., Medlyn, B. E., Meyer, W. S., Norton, A. J., Owens, J., Pitman, A., Pendall, E., Prober, S. M., Ray, R. L., Restrepo-Coupe, N., Rifai, S. W., Rowlings, D., Schipper, L., Silberstein, R. P., Teckentrup, L., Thompson, S. E., Ukkola, A. M., Wall, A., Wang, Y. P., Wardlaw, T. J., and Woodgate, W.: Bridge to the future: Important lessons from 20 years of ecosystem observations made by the OzFlux network, Glob Chang Biol, 28, 3489–3514, https://doi.org/10.1111/gcb.16141, 2022.

Cao, S., Li, M., Zhu, Z., Wang, Z., Zha, J., Zhao, W., Duanmu, Z., Chen, J., Zheng, Y., Chen, Y., Myneni, R. B., and Piao, S.: Spatiotemporally consistent global dataset of the GIMMS leaf area index (GIMMS LAI4g) from 1982 to 2020, Earth Syst. Sci. Data, 15, 4877–4899, https://doi.org/10.5194/essd-15-4877-2023, 2023.

Chen, J. M., Ju, W., Ciais, P., Viovy, N., Liu, R., Liu, Y., and Lu, X.: Vegetation structural change since 1981 significantly enhanced the terrestrial carbon sink, Nat. Commun., 10, 4259, https://doi.org/10.1038/s41467-019-12257-8, 2019.

Cheng, J., Liang, S., Verhoef, W., Shi, L., and Liu, Q.: Estimating the hemispherical broadband longwave emissivity of global vegetated surfaces using a radiative transfer model, IEEE Trans. Geosci. Remote Sens., 54, 905–917, https://doi.org/10.1109/TGRS.2015.2469535, 2016.

Chu, H., Christianson, D. S., Cheah, Y.-W., Pastorello, G., O'Brien, F., Geden, J., Ngo, S.-T., Hollowgrass, R., Leibowitz, K., Beekwilder, N. F., Sandesh, M., Dengel, S., Chan, S. W., Santos, A., Delwiche, K., Yi, K., Buechner, C., Baldocchi, D., Papale, D., Keenan, T. F., Biraud, S. C., Agarwal, D. A., and Torn, M. S.: AmeriFlux BASE data pipeline to support network growth and data sharing, Sci Data, 10, 614, https://doi.org/10.1038/s41597-023-02531-2, 2023.

Cui, J., Lian, X., Huntingford, C., Gimeno, L., Wang, T., Ding, J., He, M., Xu, H., Chen, A., Gentine, P., and Piao, S.: Global water availability boosted by vegetation-driven changes in atmospheric moisture transport, Nature Geoscience, https://doi.org/10.1038/s41561-022-01061-7, 2022.

van Dijk, A. I. J. M. and Bruijnzeel, L. A.: Modelling rainfall interception by vegetation of variable density using an adapted analytical model. Part 2. Model validation for a tropical upland mixed cropping system, Journal of Hydrology, 247, 239–262, https://doi.org/10.1016/S0022-1694(01)00393-6, 2001.

Endsley, K. A., Zhao, M., Kimball, J. S., Albrethsen, T., and Devadiga, S.: Improved global estimates of terrestrial evapotranspiration using the MODIS and VIIRS sensors, J. Hydrometeorol., 26, 817–833, https://doi.org/10.1175/JHM-D-24-0145.1, 2025.

Feng, J., Zhang, K., Chao, L., Zhan, H., and Li, Y.: P-LSHv2: a multi-decadal global daily evapotranspiration dataset enhanced with explicit soil moisture constraints, Earth Syst. Sci. Data, 17, 5039–5064, https://doi.org/10.5194/essd-17-5039-2025, 2025.

Friedl, M. and Sulla-Menashe, D.: MODIS/Terra+Aqua Land Cover Type Yearly L3 Global 500m SIN Grid V061, https://doi.org/10.5067/MODIS/MCD12Q1.061, 2022.

Gan, R., Zhang, Y., Shi, H., Yang, Y., Eamus, D., Cheng, L., Chiew, F. H. S., and Yu, Q.: Use of satellite leaf area index estimating evapotranspiration and gross assimilation for Australian ecosystems, Ecohydrology, 11, e1974, https://doi.org/10.1002/eco.1974, 2018.

Gorelick, N., Hancher, M., Dixon, M., Ilyushchenko, S., Thau, D., and Moore, R.: Google Earth Engine: Planetary-scale geospatial analysis for everyone, Remote Sens. Environ., 202, 18–27, https://doi.org/10.1016/j.rse.2017.06.031, 2017.

Harper, K. L., Lamarche, C., Hartley, A., Peylin, P., Ottlé, C., Bastrikov, V., San Martín, R., Bohnenstengel, S. I., Kirches, G., Boettcher, M., Shevchuk, R., Brockmann, C., and Defourny, P.: A 29-year time series of annual 300m resolution plant-functional-type maps for climate models, Earth Syst. Sci. Data, 15, 1465–1499, https://doi.org/10.5194/essd-15-1465-2023, 2023.

Harris, I., Osborn, T. J., Jones, P., and Lister, D.: Version 4 of the CRU TS monthly high-resolution gridded multivariate climate dataset, Sci Data, 7, 109, https://doi.org/10.1038/s41597-020-0453-3, 2020.

He, S., Zhang, Y., Ma, N., Tian, J., Kong, D., and Liu, C.: A daily and 500m coupled evapotranspiration and gross primary production product across China during 2000–2020, Earth System Science Data, 14, 5463–5488, https://doi.org/10.5194/essd-14-5463-2022, 2022.

Heiskanen, J., Brümmer, C., Buchmann, N., Calfapietra, C., Chen, H., Gielen, B., Gkritzalis, T., Hammer, S., Hartman, S., Herbst, M., Janssens, I. A., Jordan, A., Juurola, E., Karstens, U., Kasurinen, V., Kruijt, B., Lankreijer, H., Levin, I., Linderson, M.-L., Loustau, D., Merbold, L., Myhre, C. L., Papale, D., Pavelka, M., Pilegaard, K., Ramonet, M., Rebmann, C., Rinne, J., Rivier, L., Saltikoff, E., Sanders, R., Steinbacher, M., Steinhoff, T., Watson, A., Vermeulen, A. T., Vesala, T., Vítková, G., and Kutsch, W.: The integrated carbon observation system in Europe, https://doi.org/10.1175/BAMS-D-19-0364.1, 2022.

Hoek van Dijke, A. J., Herold, M., Mallick, K., Benedict, I., Machwitz, M., Schlerf, M., Pranindita, A., Theeuwen, J. J. E., Bastin, J.-F., and Teuling, A. J.: Shifts in regional water availability due to global tree restoration, Nature Geoscience, 15, 363–368, https://doi.org/10.1038/s41561-022-00935-0, 2022.

Huffman, G. J.: GPCP precipitation level 3 monthly 0.5-degree V3.3, https://doi.org/10.5067/MEASURES/GPCP/DATA306, 2024.

Humphrey, V. and Gudmundsson, L.: GRACE-REC: a reconstruction of climate-driven water storage changes over the last century, Earth Syst. Sci. Data, 11, 1153–1170, https://doi.org/10.5194/essd-11-1153-2019, 2019.

Icos Ri, Aalto, J., Aalto, P., Aaltonen, H., Aiguier, T., Akubia, J., Ala-Könni, J., Alivernini, A., Alonso, L., Aluome, C., Andersson, T., Arriga, N., Aurela, M., Brechet, L., Baab, F., Back, J., Bagheri, S., Baltes, U., Baneschi, I., Barral, H., Barten, S., Bastos Campos, F., Baur, T., Bauters, M., Bazot, S., Beauclair, P., Becker, N., Behrens, N., Belelli Marchesini, L., Bergström, G., Bernhofer, C., Berveiller, D., Biermann, T., Bignotti, L., Biron, R., Bloor, J., Bodson, B., Boeckx, P., Boeske, L., Bogaerts, G., Bonal, D., Boon, G., Bornet, F., Bortoli, M., Boschetti, F., Bosio, I., Bresseleers, S., Brut, A., Brümmer, C., Buchmann, N., Bulonza, E., Burban, B., Burri, S., Buysse, P., Båth, A., Calandrelli, D., Calvet, J.-C., Canut-Rocafort, G., Carrara, A., Cash, J., Cavagna, M., Ceschia, E., Chabbi, A., Chan, T., Chebbi, W., Chebil, B., Chianucci, F., Chipeaux, C., Chopin, H., Christen, A., Chrysoulakis, N., Claverie, N., Cobbe, I., Cohard, J.-M., Colosse, D., Conte, A., Corsanici, R., Coulaud, C., Courtois, P., Coyle, M., Cremonese, E., Crill, P., Cuntz, M., Cuocolo, D., Czerný, R., Depuydt, J., Daelman, R., Darenová, E., Darsonville, O., De Ligne, A., De Meulder, T., De Simon, G., Decau, M.-L., Dejosez, S., Dell'Acqua, A., Delorme, J.-P., Delpierre, N., Demoulin, L., Denou, J.-L., et al.: Ecosystem final quality (L2) product in ETC-archive format - release 2025-1, https://doi.org/10.18160/S6HM-CP8Q, 5 May 2025.

Isaac, P., Cleverly, J., McHugh, I., van Gorsel, E., Ewenz, C., and Beringer, J.: OzFlux data: network integration from collection to curation, Biogeosciences, 14, 2903–2928, https://doi.org/10.5194/bg-14-2903-2017, 2017.

Joiner, J. and Yoshida, Y.: Satellite-based reflectances capture large fraction of variability in global gross primary production (GPP) at weekly time scales, Agric. For. Meteorol., 291, 108092, https://doi.org/10.1016/j.agrformet.2020.108092, 2020.

Kim, S., Anabalón, A., and Sharma, A.: An assessment of concurrency in evapotranspiration trends across multiple global datasets, Journal of Hydrometeorology, https://doi.org/10.1175/JHM-D-20-0059.1, 2021.

Kong, D., Zhang, Y., Gu, X., and Wang, D.: A robust method for reconstructing global MODIS EVI time series on the Google Earth Engine, ISPRS Journal of Photogrammetry and Remote Sensing, 155, 13–24, https://doi.org/10.1016/j.isprsjprs.2019.06.014, 2019.

Lai, J., Kooijmans, L. M. J., Sun, W., Lombardozzi, D., Campbell, J. E., Gu, L., Luo, Y., Kuai, L., and Sun, Y.: Terrestrial photosynthesis inferred from plant carbonyl sulfide uptake, Nature, 634, 855–861, https://doi.org/10.1038/s41586-024-08050-3, 2024.

Lasslop, G., Reichstein, M., Papale, D., Richardson, A. D., Arneth, A., Barr, A., Stoy, P., and Wohlfahrt, G.: Separation of net ecosystem exchange into assimilation and respiration using a light response curve approach: critical issues and global evaluation, Global Change Biology, 16, 187–208, https://doi.org/10.1111/j.1365-2486.2009.02041.x, 2010.

Leng, J., Chen, J. M., Li, W., Luo, X., Xu, M., Liu, J., Wang, R., Rogers, C., Li, B., and Yan, Y.: Global datasets of hourly carbon and water fluxes simulated using a satellite-based process model with dynamic parameterizations, Earth Syst. Sci. Data, 16, 1283–1300, https://doi.org/10.5194/essd-16-1283-2024, 2024.

https://doi.org/10.5194/essd-2026-94
Preprint. Discussion started: 2 March 2026

Lesk, C. S., Winter, J. M., and Mankin, J. S.: Projected runoff declines from plant physiological effects on precipitation, Nat. Water, 3, 167–177, https://doi.org/10.1038/s44221-024-00361-z, 2025.

Leuning, R., Zhang, Y. Q., Rajaud, A., Cleugh, H., and Tu, K.: A simple surface conductance model to estimate regional evaporation using MODIS leaf area index and the Penman-Monteith equation, Water Resour. Res., 44, https://doi.org/10.1029/2007wr006562, 2008.

Li, B., Ryu, Y., Jiang, C., Dechant, B., Liu, J., Yan, Y., and Li, X.: BESSv2.0: a satellite-based and coupled-process model for quantifying long-term global land–atmosphere fluxes, Remote Sens. Environ., 295, 113696, https://doi.org/10.1016/j.rse.2023.113696, 2023a.

Li, F., Xiao, J., Chen, J., Ballantyne, A., Jin, K., Li, B., Abraha, M., and John, R.: Global water use efficiency saturation due to increased vapor pressure deficit, Science, 381, 672–677, https://doi.org/10.1126/science.adf5041, 2023b.

Li, X. and Xiao, J.: Mapping photosynthesis solely from solar-induced chlorophyll fluorescence: a global, fine-resolution dataset of gross primary production derived from OCO-2, Remote Sens., 11, 2563, https://doi.org/10.3390/rs11212563, 2019.

Liang, S., Cheng, J., Jia, K., Jiang, B., Liu, Q., Xiao, Z., Yao, Y., Yuan, W., Zhang, X., Zhao, X., and Zhou, J.: The global land surface satellite (GLASS) product suite, https://doi.org/10.1175/BAMS-D-18-0341.1, 2021.

Liu, N. F., Liu, Q., Wang, L. Z., Liang, S. L., Wen, J. G., Qu, Y., and Liu, S. H.: A statistics-based temporal filter algorithm to map spatiotemporally continuous shortwave albedo from MODIS data, Hydrol. Earth Syst. Sci., 17, 2121–2129, https://doi.org/10.5194/hess-17-2121-2013, 2013a.

Liu, S., Li, X., Xu, Z., Che, T., Xiao, Q., Ma, M., Liu, Q., Jin, R., Guo, J., Wang, L., Wang, W., Qi, Y., Li, H., Xu, T., Ran, Y., Hu, X., Shi, S., Zhu, Z., Tan, J., Zhang, Y., and Ren, Z.: The heihe integrated observatory network: a basin-scale land surface processes observatory in China, Vadose Zone J., 17, 180072, https://doi.org/10.2136/vzj2018.04.0072, 2018.

Liu, S. M., Xu, Z. W., Zhu, Z. L., Jia, Z. Z., and Zhu, M. J.: Measurements of evapotranspiration from eddy-covariance systems and large aperture scintillometers in the hai river basin, china, J. Hydrol., 487, 24–38, https://doi.org/10.1016/j.jhydrol.2013.02.025, 2013b.

Loomis, B. D., Luthcke, S. B., and Sabaka, T. J.: Regularization and error characterization of GRACE mascons, J. Geod., 93, 1381–1398, https://doi.org/10.1007/s00190-019-01252-y, 2019.

Ma, N., Szilagyi, J., and Zhang, Y.: Calibration-free complementary relationship estimates terrestrial evapotranspiration globally, Water Resour. Res., 57, e2021WR029691, https://doi.org/10.1029/2021WR029691, 2021.

Ma, N., Zhang, Y., and Szilagyi, J.: Water-balance-based evapotranspiration for 56 large river basins: a benchmarking dataset for global terrestrial evapotranspiration modeling, J. Hydrol., 630, 130607, https://doi.org/10.1016/j.jhydrol.2024.130607, 2024.

Ma, Y., Hu, Z., Xie, Z., Ma, W., Wang, B., Chen, X., Li, M., Zhong, L., Sun, F., Gu, L., Han, C., Zhang, L., Liu, X., Ding, Z., Sun, G., Wang, S., Wang, Y., and Wang, Z.: A long-term (2005–2016) dataset of hourly integrated land–atmosphere interaction observations on the Tibetan Plateau, Earth Syst. Sci. Data, 12, 2937–2957, https://doi.org/10.5194/essd-12-2937-2020, 2020.

Medlyn, B. E., Duursma, R. A., Eamus, D., Ellsworth, D. S., Prentice, I. C., Barton, C. V. M., Crous, K. Y., De Angelis, P., Freeman, M., and Wingate, L.: Reconciling the optimal and empirical approaches to modelling stomatal conductance, Global Change Biol., 17, 2134–2144, https://doi.org/10.1111/j.1365-2486.2010.02375.x, 2011.

Miralles, D. G., Bonte, O., Koppa, A., Baez-Villanueva, O. M., Tronquo, E., Zhong, F., Beck, H. E., Hulsman, P., Dorigo, W., Verhoest, N. E. C., and Haghdoost, S.: GLEAM4: global land evaporation and soil moisture dataset at 0.1° resolution from 1980 to near present, Sci. Data, 12, 416, https://doi.org/10.1038/s41597-025-04610-y, 2025.

Mu, Q., Zhao, M., and Running, S. W.: Improvements to a MODIS global terrestrial evapotranspiration algorithm, Remote Sens. Environ., 115, 1781–1800, https://doi.org/10.1016/j.rse.2011.02.019, 2011.

Myneni, R., Knyazikhin, Y., and Park, T.: MODIS/terra leaf area index/FPAR 8-day L4 global 500m SIN grid V061, https://doi.org/10.5067/MODIS/MOD15A2H.061, 2021.

Nelson, J. A., Walther, S., Gans, F., Kraft, B., Weber, U., Novick, K., Buchmann, N., Migliavacca, M., Wohlfahrt, G., Šigut, L., Ibrom, A., Papale, D., Göckede, M., Duveiller, G., Knohl, A., Hörtnagl, L., Scott, R. L., Dušek, J., Zhang, W., Hamdi, Z. M., Reichstein, M., Aranda-Barranco, S., Ardö, J., Op de Beeck, M., Billesbach, D., Bowling, D., Bracho, R., Brümmer, C., Camps-Valls, G., Chen, S., Cleverly, J. R., Desai, A., Dong, G., El-Madany, T. S., Euskirchen, E. S., Feigenwinter, I., Galvagno, M., Gerosa, G. A., Gielen, B., Goded, I., Goslee, S., Gough, C. M., Heinesch, B., Ichii, K., Jackowicz-Korczynski, M. A., Klosterhalfen, A., Knox, S., Kobayashi, H., Kohonen, K.-M., Korkiakoski, M., Mammarella, I., Gharun, M., Marzuoli, R., Matamala, R., Metzger, S., Montagnani, L., Nicolini, G., O'Halloran, T., Ourcival, J.-M., Peichl, M., Pendall, E., Ruiz Reverter, B., Roland, M., Sabbatini, S., Sachs, T., Schmidt, M., Schwalm, C. R., Shekhar, A., Silberstein, R., Silveira, M. L., Spano, D., Tagesson, T., Tramontana, G., Trotta, C., Turco, F., Vesala, T., Vincke, C., Vitale, D., Vivoni, E. R., Wang, Y., Woodgate, W., Yepez, E. A., Zhang, J., Zona, D., and Jung, M.: X-BASE: the first terrestrial carbon and water flux products from an extended data-driven scaling framework, FLUXCOM-X, Biogeosciences, 21, 5079–5115, https://doi.org/10.5194/bg-21-5079-2024, 2024.

Novick, K. A., Biederman, J. A., Desai, A. R., Litvak, M. E., Moore, D. J. P., Scott, R. L., and Torn, M. S.: The AmeriFlux network: a coalition of the willing, Agric. For. Meteorol., 249, 444–456, https://doi.org/10.1016/j.agrformet.2017.10.009, 2018.

Oki, T.: Global Hydrological Cycles and World Water Resources, Science, 313, 1068–1072, https://doi.org/10.1126/science.1128845, 2006.

Pastorello, G., Trotta, C., Canfora, E., Chu, H., Christianson, D., Cheah, Y. W., Poindexter, C., Chen, J., Elbashandy, A., Humphrey, M., Isaac, P., Polidori, D., Reichstein, M., Ribeca, A., van Ingen, C., Vuichard, N., Zhang, L., Amiro, B., Ammann, C., Arain, M. A., Ardo, J., Arkebauer, T., Arndt, S. K., Arriga, N., Aubinet, M., Aurela, M., Baldocchi, D., Barr, A., Beamesderfer, E., Marchesini, L. B., Bergeron, O., Beringer, J., Bernhofer, C., Berveiller, D., Billesbach, D., Black, T. A., Blanken, P. D., Bohrer, G., Boike, J., Bolstad, P. V., Bonal, D., Bonnefond, J. M., Bowling, D. R., Bracho, R., Brodeur, J., Brummer, C., Buchmann, N., Burban, B., Burns, S. P., Buysse, P., Cale, P., Cavagna, M., Cellier, P., Chen, S., Chini, I., Christensen, T. R., Cleverly, J., Collalti, A., Consalvo, C., Cook, B. D., Cook, D., Coursolle, C., Cremonese, E., Curtis, P. S., D'Andrea, E., da Rocha, H., Dai, X., Davis, K. J., Cinti, B., Grandcourt, A., Ligne, A., De Oliveira, R. C., Delpierre, N., Desai, A. R., Di Bella, C. M., Tommasi, P. D., Dolman, H., Domingo, F., Dong, G., Dore, S., Duce, P., Dufrene, E., Dunn, A., Dusek, J., Eamus, D., Eichelmann, U., ElKhidir, H. A. M., Eugster, W., Ewenz, C. M., Ewers, B., Famulari, D., Fares, S., Feigenwinter, I., Feitz, A., Fensholt, R., Filippa, G., Fischer, M., Frank, J., Galvagno, M., et al.: The FLUXNET2015 dataset and the ONEFlux processing pipeline for eddy covariance data, Sci Data, 7, 225, https://doi.org/10.1038/s41597-020-0534-3, 2020.

Reichstein, M., Falge, E., Baldocchi, D., Papale, D., Aubinet, M., Berbigier, P., Bernhofer, C., Buchmann, N., Gilmanov, T., Granier, A., Grünwald, T., Havránková, K., Ilvesniemi, H., Janous, D., Knohl, A., Laurila, T., Lohila, A., Loustau, D., Matteucci, G., Meyers, T., Miglietta, F., Ourcival, J.-M., Pumpanen, J., Rambal, S., Rotenberg, E., Sanz, M., Tenhunen, J., Seufert, G., Vaccari, F., Vesala, T., Yakir, D., and Valentini, R.: On the separation of net ecosystem exchange into assimilation and ecosystem respiration: review and improved algorithm, Global Change Biology, 11, 1424–1439, https://doi.org/10.1111/j.1365-2486.2005.001002.x, 2005.

Running, S., Mu, Q., and Zhao, M.: MOD17A2H MODIS/terra gross primary productivity 8-day L4 global 500m SIN grid V006, https://doi.org/10.5067/MODIS/MOD17A2H.006, 2015.

Running, S. W., Nemani, R. R., Heinsch, F. A., Zhao, M., Reeves, M., and Hashimoto, H.: A continuous satellite-derived measure of global terrestrial primary production, Bioscience, 54, 547–560, https://doi.org/10.1641/0006-3568(2004)054%255B0547:ACSMOG%255D2.0.CO;2, 2004.

Save, H.: CSR GRACE and GRACE-FO RL06 mascon solutions v02, https://doi.org/10.15781/cgq9-nh24., 2022.

Save, H., Bettadpur, S., and Tapley, B. D.: High-resolution CSR GRACE RL05 mascons, JGR Solid Earth, 121, 7547–7569, https://doi.org/10.1002/2016JB013007, 2016.

Schaaf, C. and Wang, Z.: MODIS/Terra+Aqua BRDF/Albedo Daily L3 Global - 500m V061, https://doi.org/10.5067/MODIS/MCD43A3.061, 2021.

Schneider, U., Hänsel, S., Finger, P., Rustemeier, E., and Ziese, M.: GPCC full data monthly version 2022 at 0.5°: monthly land-surface precipitation from rain-gauges built on GTS-based and historic data: globally gridded monthly totals (2022), https://doi.org/10.5676/DWD_GPCC/FD_M_V2022_050, 2022.

Tagesson, T., Tian, F., Schurgers, G., Horion, S., Scholes, R., Ahlström, A., Ardö, J., Moreno, A., Madani, N., Olin, S., and Fensholt, R.: A physiology-based earth observation model indicates stagnation in the global gross primary production during recent decades, Global Change Biol., 27, 836–854, https://doi.org/10.1111/gcb.15424, 2021.

Teluguntla, P., Thenkabail, P., Oliphant, A., Gumma, M., Aneece, I., Foley, D., and McCormick, R.: Landsat-derived global rainfed and irrigated-cropland product 30 m V001, https://doi.org/10.5067/COMMUNITY/LGRIP/LGRIP30.001, 2023.

Ueyama, M., Takao, Y., Yazawa, H., Tanaka, M., Yabuki, H., Kumagai, T., Iwata, H., Awal, M. A., Du, M., Harazono, Y., Hata, Y., Hirano, T., Hiura, T., Ide, R., Ishida, S., Ishikawa, M., Kitamura, K., Kominami, Y., Komiya, S., Kotani, A., Inoue, Y., Machimura, T., Matsumoto, K., Matsuura, Y., Mizoguchi, Y., Murayama, S., Nagano, H., Nakai, T., Nakaji, T., Nakaya, K., Ohkubo, S., Ohta, T., Ono, K., Saitoh, T. M., Sakabe, A., Shimizu, T., Shimoda, S., Sugita, M., Takagi, K., Takahashi, Y., Takamura, N., Takanashi, S., Takimoto, T., Yasuda, Y., Wang, Q., Asanuma, J., Hasegawa, H., Hiyama, T., Iijima, Y., Ishidoya, S., Itoh, M., Kato, T., Kondo, H., Kosugi, Y., Kume, T., Maeda, T., Matsuura, S., Maximov, T., Miyama, T., Moriwaki, R., Muraoka, H., Petrov, R., Suzuki, J., Taniguchi, S., and Ichii, K.: The JapanFlux2024 dataset for eddy covariance observations covering japan and east Asia from 1990 to 2023, Earth Syst. Sci. Data, 17, 3807–3833, https://doi.org/10.5194/essd-17-3807-2025, 2025.

Viney, N., Perraud, J., Vaze, J., Chiew, F., Post, D., and Yang, A.: The usefulness of bias constraints in model calibration for regionalisation to ungauged catchments, 18th World IMACS Congress and MODSIM09 International Congress on Modelling and Simulation, Cairns, Australia, 13–17, 2009.

Wan, Z., Hook, S., and Hulley, G.: MODIS/terra land surface temperature/emissivity 8-day L3 global 1km SIN grid V061, https://doi.org/10.5067/MODIS/MOD11A2.061, 2021.

Wang, F., Chen, J. M., Gonsamo, A., Zhou, B., Cao, F., and Yi, Q.: A two-leaf rectangular hyperbolic model for estimating GPP across vegetation types and climate conditions, J. Geophys. Res.: Biogeosci., 119, 1385–1398, https://doi.org/10.1002/2013JG002596, 2014.

Wang, J., Tang, R., Liu, M., Jiang, Y., Huang, L., and Li, Z.-L.: Coordinated estimates of 4-day 500 m global land surface energy balance components, Remote Sens. Environ., 326, 114795, https://doi.org/10.1016/j.rse.2025.114795, 2025.

Wang, J., Tang, R., Liu, M., and Li, Z.-L.: Energy-conservation datasets of global land surface radiation and heat fluxes from 2000–2020 generated by CoSEB, Earth Syst. Sci. Data, 18, 443–463, https://doi.org/10.5194/essd-18-443-2026, 2026.

Wang, S., Zhang, Y., Ju, W., Qiu, B., and Zhang, Z.: Tracking the seasonal and inter-annual variations of global gross primary production during last four decades using satellite near-infrared reflectance data, Sci. Total Environ., 755, 142569, https://doi.org/10.1016/j.scitotenv.2020.142569, 2021.

Wang, Z., Peñuelas, J., Tagesson, T., Smith, W. K., Wu, M., He, W., Sitch, S., and Wang, S.: Evolution of global terrestrial gross primary productivity trend, Ecosyst. Health Sustainability, https://doi.org/10.34133/ehs.0278, 2024.

Warm Winter 2020 Team, ICOS Ecosystem Thematic Centre, ICOS Ecosystem Thematic Centre, and Trotta, C.: Warm winter 2020 ecosystem eddy covariance flux product for 73 stations in FLUXNET-archive format—release 2022-1, https://doi.org/10.18160/2G60-ZHAK, 1 February 2022.

Watkins, M. M., Wiese, D. N., Yuan, D.-N., Boening, C., and Landerer, F. W.: Improved methods for observing Earth's time variable mass distribution with GRACE using spherical cap mascons, Journal of Geophysical Research: Solid Earth, 120, 2648–2671, https://doi.org/10.1002/2014jb011547, 2015.

Wei, H., Zhang, Y., Huang, Q., Chiew, F. H. S., Luan, J., Xia, J., and Liu, C.: Direct vegetation response to recent CO2 rise shows limited effect on global streamflow, Nat Commun, 15, 9423, https://doi.org/10.1038/s41467-024-53879-x, 2024.

Wei, H., Zhang, Y., Huang, Q., Liu, C., and Wagener, T.: Functional relationships reveal large differences in streamflow response to eCO2-vegetation in global water models, Geophys. Res. Lett., 52, e2024GL113685, https://doi.org/10.1029/2024GL113685, 2025.

Wiese, D. N., Landerer, F. W., and Watkins, M. M.: Quantifying and reducing leakage errors in the JPL RL05M GRACE mascon solution, Water Resour. Res., 52, 7490–7502, https://doi.org/10.1002/2016wr019344, 2016.

Wiese, D. N., Yuan, D. N., Boening, C., Landerer, F. W., and Watkins: JPL GRACE mascon ocean, ice, and hydrology equivalent water height release 06 Coastal Resolution Improvement (CRI) filtered version 1.0., https://doi.org/10.5067/TEMSC-3MJC6, 2018.

World Meteorological Organization (WMO): State of global water resources report 2024, 2025.

Wutzler, T., Lucas-Moffat, A., Migliavacca, M., Knauer, J., Sickel, K., Šigut, L., Menzer, O., and Reichstein, M.: Basic and extensible post-processing of eddy covariance flux data with REddyProc, Biogeosciences, 15, 5015–5030, https://doi.org/10.5194/bg-15-5015-2018, 2018.

Xiao, X., Zhang, Q., Braswell, B., Urbanski, S., Boles, S., Wofsy, S., Moore, B., and Ojima, D.: Modeling gross primary production of temperate deciduous broadleaf forest using satellite images and climate data, Remote Sens. Environ., 91, 256–270, https://doi.org/10.1016/j.rse.2004.03.010, 2004.

Xie, Y., Kong, D., Zhang, Y., Zhong, Y., Ma, N., Gong, R., Ci, H., Xiao, M., and Gu, X.: Evaluation of the performance of multiple reanalysis forcing data in potential evapotranspiration estimation and its implication for actual evapotranspiration modeling, J. Hydrol., 660, 133472, https://doi.org/10.1016/j.jhydrol.2025.133472, 2025.

Xu, Z., Zhang, Y., and Kong, D.: PML-V2.2: Global terrestrial evapotranspiration and gross primary production dataset from 1982 to near present, National Tibetan Plateau / Third Pole Environment Data Center, https://doi.org/10.11888/Terre.tpdc.303314, 2026.

Yan, K., Pu, J., Park, T., Xu, B., Zeng, Y., Yan, G., Weiss, M., Knyazikhin, Y., and Myneni, R. B.: Performance stability of the MODIS and VIIRS LAI algorithms inferred from analysis of long time series of products, Remote Sens. Environ., 260, 112438, https://doi.org/10.1016/j.rse.2021.112438, 2021.

Yan, Y., Li, B., Dechant, B., Xu, M., Luo, X., Qu, S., Miao, G., Leng, J., Shang, R., Shu, L., Jiang, C., Wang, H., Jeong, S., Ryu, Y., and Chen, J. M.: Plant traits shape global spatiotemporal variations in photosynthetic efficiency, Nat. Plants, 11, 924–934, https://doi.org/10.1038/s41477-025-01958-2, 2025.

Yang, R., Wang, J., Zeng, N., Sitch, S., Tang, W., McGrath, M. J., Cai, Q., Liu, D., Lombardozzi, D., Tian, H., Jain, A. K., and Han, P.: Divergent historical GPP trends among state-of-the-art multi-model simulations and satellite-based products, Earth Syst. Dyn., 13, 833–849, https://doi.org/10.5194/esd-13-833-2022, 2022.

Yang, Y., Roderick, M. L., Guo, H., Miralles, D. G., Zhang, L., Fatichi, S., Luo, X., Zhang, Y., McVicar, T. R., Tu, Z., Keenan, T. F., Fisher, J. B., Gan, R., Zhang, X., Piao, S., Zhang, B., and Yang, D.: Evapotranspiration on a greening Earth, Nat Rev Earth Environ, 4, 626–641, https://doi.org/10.1038/s43017-023-00464-3, 2023.

Yao, Y., Liang, S., Cheng, J., Liu, S., Fisher, J. B., Zhang, X., Jia, K., Zhao, X., Qin, Q., Zhao, B., Han, S., Zhou, G., Zhou, G., Li, Y., and Zhao, S.: MODIS-driven estimation of terrestrial latent heat flux in China based on a modified Priestley–Taylor algorithm, Agricultural and Forest Meteorology, 171–172, 187–202, https://doi.org/10.1016/j.agrformet.2012.11.016, 2013.

Yao, Y., Liang, S., Li, X., Hong, Y., Fisher, J. B., Zhang, N., Chen, J., Cheng, J., Zhao, S., Zhang, X., Jiang, B., Sun, L., Jia, K., Wang, K., Chen, Y., Mu, Q., and Feng, F.: Bayesian multimodel estimation of global terrestrial latent heat flux from eddy covariance, meteorological, and satellite observations, Journal of Geophysical Research: Atmospheres, 119, 4521–4545, https://doi.org/10.1002/2013JD020864, 2014.

Yebra, M., Van Dijk, A., Leuning, R., Huete, A., and Guerschman, J. P.: Evaluation of optical remote sensing to estimate actual evapotranspiration and canopy conductance, Remote Sens. Environ., 129, 250–261, https://doi.org/10.1016/j.rse.2012.11.004, 2013.

Yu, G.-R., Wen, X.-F., Sun, X.-M., Tanner, B. D., Lee, X., and Chen, J.-Y.: Overview of ChinaFLUX and evaluation of its eddy covariance measurement, Agric. For. Meteorol., 137, 125–137, https://doi.org/10.1016/j.agrformet.2006.02.011, 2006.

Yu, G.-R., Chen, Z., and Wang, Y.-P.: Carbon, water and energy fluxes of terrestrial ecosystems in China, Agricultural and Forest Meteorology, 346, 109890, https://doi.org/10.1016/j.agrformet.2024.109890, 2024.

Yu, L., Qiu, G. Y., Yan, C., Zhao, W., Zou, Z., Ding, J., Qin, L., and Xiong, Y.: A global terrestrial evapotranspiration product based on the three-temperature model with fewer input parameters and no calibration requirement, Earth Syst. Sci. Data, 14, 3673–3693, https://doi.org/10.5194/essd-14-3673-2022, 2022.

Yuan, Q., Wang, X., Che, T., and Li, J.: Global carbon flux dataset generated by fusing remote sensing and multiple flux networks observation, Sci. Data, 12, 1359, https://doi.org/10.1038/s41597-025-05672-8, 2025a.

Yuan, W., Liu, S., Yu, G., Bonnefond, J.-M., Chen, J., Davis, K., Desai, A. R., Goldstein, A. H., Gianelle, D., Rossi, F., Suyker, A. E., and Verma, S. B.: Global estimates of evapotranspiration and gross primary production based on MODIS and global meteorology data, Remote Sensing of Environment, 114, 1416–1431, https://doi.org/10.1016/j.rse.2010.01.022, 2010.

Yuan, W., Tian, J., Wang, M., Wang, S., Xu, W., Wang, Y., Fu, Z., Girardin, M. P., Green, J. K., Zhou, S., Shang, J., He, B., Huang, M., Liu, M., Lu, H., Piao, S., Qing, Y., Xue, M., Song, C., Su, Y., Sadok, W., Zhang, Y., and Chen, X.: Impacts of rising atmospheric dryness on terrestrial ecosystem carbon cycle, Nat. Rev. Earth Environ., 6, 712–727, https://doi.org/10.1038/s43017-025-00726-2, 2025b.

https://doi.org/10.5194/essd-2026-94
Preprint. Discussion started: 2 March 2026

Zhang, K., Kimball, J. S., and Running, S. W.: A review of remote sensing based actual evapotranspiration estimation, Wires Water, 3, 834–853, https://doi.org/10.1002/wat2.1168, 2016a.

Zhang, K., Chen, H., Ma, N., Shang, S., Wang, Y., Xu, Q., and Zhu, G.: A global dataset of terrestrial evapotranspiration and soil moisture dynamics from 1982 to 2020, Sci. Data, 11, 445, https://doi.org/10.1038/s41597-024-03271-7, 2024.

Zhang, X., Zhang, Y., Ma, N., Kong, D., Tian, J., Shao, X., and Tang, Q.: Greening-induced increase in evapotranspiration over Eurasia offset by CO2-induced vegetational stomatal closure, Environ. Res. Lett., 16, 124008, https://doi.org/10.1088/1748-9326/ac3532, 2021.

Zhang, X., Zhang, Y., Tian, J., Ma, N., and Wang, Y.-P.: CO2 fertilization is spatially distinct from stomatal conductance reduction in controlling ecosystem water-use efficiency increase, Environ. Res. Lett., 17, 054048, https://doi.org/10.1088/1748-9326/ac6c9c, 2022.

Zhang, Y., Chiew, F. H. S., Zhang, L., Leuning, R., and Cleugh, H. A.: Estimating catchment evaporation and runoff using MODIS leaf area index and the Penman-Monteith equation, Water Resour. Res., 44, https://doi.org/10.1029/2007wr006563, 2008.

Zhang, Y., Leuning, R., Hutley, L. B., Beringer, J., McHugh, I., and Walker, J. P.: Using long-term water balances to parameterize surface conductances and calculate evaporation at 0.05° spatial resolution, Water Resour. Res., 46, n/a-n/a, https://doi.org/10.1029/2009wr008716, 2010.

Zhang, Y., Zheng, H., Chiew, F. H. S., Arancibia, J. P.-, and Zhou, X.: Evaluating regional and global hydrological models against streamflow and evapotranspiration measurements, https://doi.org/10.1175/JHM-D-15-0107.1, 2016b.

Zhang, Y., Peña-Arancibia, J. L., McVicar, T. R., Chiew, F. H. S., Vaze, J., Liu, C., Lu, X., Zheng, H., Wang, Y., Liu, Y. Y., Miralles, D. G., and Pan, M.: Multi-decadal trends in global terrestrial evapotranspiration and its components, Scientific Reports, 6, 19124, https://doi.org/10.1038/srep19124, 2016c.

Zhang, Y., Xiao, X., Wu, X., Zhou, S., Zhang, G., Qin, Y., and Dong, J.: A global moderate resolution dataset of gross primary production of vegetation for 2000–2016, Sci. Data, 4, 170165, https://doi.org/10.1038/sdata.2017.165, 2017.

Zhang, Y., Kong, D., Gan, R., Chiew, F. H. S., McVicar, T. R., Zhang, Q., and Yang, Y.: Coupled estimation of 500 m and 8-day resolution global evapotranspiration and gross primary production in 2002–2017, Remote Sens. Environ., 222, 165–182, https://doi.org/10.1016/j.rse.2018.12.031, 2019.

Zhang, Y., Li, C., Chiew, F. H. S., Post, D. A., Zhang, X., Ma, N., Tian, J., Kong, D., Leung, L. R., Yu, Q., Shi, J., and Liu, C.: Southern Hemisphere dominates recent decline in global water availability, Science, 382, 579–584, https://doi.org/10.1126/science.adh0716, 2023.

Zhang, Y., Blöschl, G., Wei, H., Kong, D., Ma, N., Wagener, T., Tian, J., Xia, J., Li, C., Wang, L., Chiew, F. H. S., Leung, L. R., Liu, X., Zheng, H., Zhang, X., and Liu, C.: Overestimation of past and future increases in global river flow by Earth system models, Nat. Geosci., 0–10, https://doi.org/10.1038/s41561-025-01897-9, 2026.

Zhao, G., Li, Y., Zhou, L., and Gao, H.: Evaporative water loss of 1.42 million global lakes, Nat. Commun., 13, 3686, https://doi.org/10.1038/s41467-022-31125-6, 2022a.

Zhao, M., A, G., Liu, Y., and Konings, A. G.: Evapotranspiration frequently increases during droughts, Nat. Clim. Change, https://doi.org/10.1038/s41558-022-01505-3, 2022b.

https://doi.org/10.5194/essd-2026-94
Preprint. Discussion started: 2 March 2026

Zheng, C., Jia, L., and Hu, G.: Global land surface evapotranspiration monitoring by ETMonitor model driven by multi-source satellite earth observations, Journal of Hydrology, 613, 128444, https://doi.org/10.1016/j.jhydrol.2022.128444, 2022.

Zheng, Y., Shen, R., Wang, Y., Li, X., Liu, S., Liang, S., Chen, J. M., Ju, W., Zhang, L., and Yuan, W.: Improved estimate of global gross primary production for reproducing its long-term variation, 1982–2017, Earth Syst. Sci. Data, 12, 2725–2746, https://doi.org/10.5194/essd-12-2725-2020, 2020.

Zhou, Y., Zhang, Y., Zhu, T., and Ju, W.: A dataset of carbon and water fluxes in the cropland ecosystem at Jurong Station (2015-2020), China Sci. Data, 8, https://doi.org/10.11922/11-6035.csd.2023.0072.zh, 2023.

Zhu, Z., Bi, J., Pan, Y., Ganguly, S., Anav, A., Xu, L., Samanta, A., Piao, S., Nemani, R. R., and Myneni, R. B.: Global data sets of vegetation leaf area index (LAI)3g and fraction of photosynthetically active radiation (FPAR)3g derived from global inventory modeling and mapping studies (GIMMS) normalized difference vegetation index (NDVI3g) for the period 1981 to 2011, Remote Sens., 5, 927–948, https://doi.org/10.3390/rs5020927, 2013.